

Optimization of process parameters in additive manufacturing based on the finite element method

Jingyi WANG and Panayiotis PAPADOPOULOS*

Department of Mechanical Engineering, University of California, Berkeley, CA, USA

Table of contents

1	Introduction	2
2	Review of continuum theory and finite element modeling	4
2.1	Continuum theory	4
2.2	Finite element modeling	6
3	Optimization problem formulation	8
4	Gradient-descent method with line search	10
5	Gradient-free Optimization Methods	13
5.1	Method of local variations	13
5.2	Bayesian optimization method	14
6	Numerical experiments	17
6.1	Two-dimensional wall after heat dissipation	17
6.2	Two-dimensional wall with hole after heat dissipation	21
7	Conclusions	28
	References	29
	Appendix A: Finite element matrices	37

Abstract

A design optimization framework for process parameters of additive manufacturing based on finite element simulation is proposed. The finite element method uses a coupled thermomechanical model developed for fused deposition modeling from the authors' previous work. Both gradient-based and gradient-free optimization methods are proposed. The gradient-based approach, which solves a PDE-constrained optimization problem, requires sensitivities computed from the fully discretized finite element model. We show the derivation of the sensitivities and apply them in a projected gradient descent algorithm. For the gradient-free approach, we propose two distinct algorithms: a local search algorithm called the method of local variations and a Bayesian optimization algorithm using Gaussian processes. To illustrate the effectiveness and differences of the methods, we provide two-dimensional design optimization examples using all three proposed algorithms.

Keywords: Additive manufacturing; sensitivity; optimization; Bayesian optimization;

*panos@berkeley.edu

1 Introduction

Additive manufacturing (AM) has enjoyed substantial success in creating parts with complex geometries, shortening the product design time and lowering costs [1, 2, 3, 4, 5, 6]. Many additive manufacturing technologies have been developed in recent years including fused deposition modeling (FDM), selective laser sintering, *etc.* AM is adopted extensively in prototyping and is increasingly deployed to industrial production of parts for the medical, aerospace and automotive industries [7, 8]. The computer simulation of the AM processes is a topic of huge interest throughout the industry and academia [9, 10, 11, 12, 13, 14, 15], where finite element method is one of the primary numerical tools used.

FDM simulation models typically solves the transient heat transfer problem during the deposition, followed by the mechanics problem based on the temperature history of a material with temperature-dependent constitutive response [10, 11, 16, 17, 18, 19, 20]. The process of deposition can be emulated using an “active/inactive” element addition approach [16, 21, 22, 23, 24, 20]. Heat transfer through conduction, convection and radiation are generally considered in simulation and the dependence of the thermal conductivity and heat capacity on temperature can be explicitly accounted for [25]. Previously, the authors proposed a fully coupled thermomechanical model for FDM [26], where the displacement and temperature fields are solved simultaneously and the deposition of new material is enabled through the creation of new elements. By accounting for existing displacement at each time step, the model can predict the quantities of interest such as maximum deformation, shape error, *etc.*

While AM simulation has progressed steadily, challenges remain in developing optimization tools for it. The optimization of process parameters of AM to achieve various design goals such as better surface finish quality, lower residual stress and less shape error for assembly is of great interest and importance [27, 28, 29, 30, 17, 19]. The process parameters to consider include chamber temperature, part orientation, printing speed, filament diameter, nozzle size and layer thickness [31, 32, 33, 34, 35]. The existing optimization tools for additive manufacturing are mostly simple, data-driven models using experimental data [1, 36, 37, 38, 39, 40]. Commonly used experiments include tensile, compression tests for the printed samples [8, 41, 42, 43, 44, 45], while dynamic mechanical tests are also performed in [46, 47]. Some of the techniques used for optimization are the Taguchi method [48, 49, 31, 50], particle swarm optimization [51] and artificial neural network (NN) [52].

In addition to experiments, an accurate finite element simulation is another natural candidate for optimization due to its flexibility and efficiency, and has been adopted by some [53]. Process mapping of the parameters can be developed using finite element simulation and subsequently applied to optimization [54, 55, 56, 57]. The finite element model used is often an uncoupled thermomechanical one with a fixed Lagrangian mesh [58, 59], which could raise the difficulty of sensitivity calculation for gradient-based optimization algorithms. The optimization variables of these studies include print speed, extrusion temperature and layer thickness [60, 61]. A purely geometric model is used in [62].

Bayesian optimization has been applied to many engineering design problems such as inverse problems [63], structural design [64] and robotics [65] with advanced technologies such as multi-fidelity surrogate models and independent constraints [66, 67]. Thus far, it has been applied to a limited extent in the optimization of AM problems [68], particularly for process parameters. Most of the approaches taken are experiment-driven or rely on geometric models, *e.g.*, part orientation optimization of AM in [69]. In [70, 71, 72], machine learning and Bayesian optimization are used for the optimization of lattice structure for metamaterials, where the stiffness of the metamaterial is computed through finite element software. A Bayesian optimization approach is adopted for the metal AM melt pool geometry optimization in [73]. A data-driven Bayesian optimization method using finite element software to generate sample points is proposed in [74]. While [75] argued for a conceptual framework to integrate experiments, finite element and machine learning together for the optimization of AM processes, the authors believe it remains a work in progress.

In most of the existing optimization methods discussed above, the simulation and optimization are largely separated. Additionally, process parameters as well as defects and uncertainty caused by the printing itself are often ignored. Further, the optimization algorithm applied might not have been systematically established and thus relies on exhaustive search. In this paper, we propose two approaches to contribute to the optimization workflow of AM process parameters, each with its own advantages. The first approach is a gradient-based optimization method, where we optimize the design objective constrained by partial differential equations (PDEs). A coupled finite element simulation model for FDM developed by the authors [26] is used, whose fully discretized form is parameterized by the optimization variables, *i.e.*, the process parameters. Then, we apply gradient-based optimization techniques to solve the optimization problem using the fully discretized sensitivities computed from the finite element model. The second approach is gradient-free and more suitable for problems where sensitivities are not easily available. We propose

two algorithms that are differentiated by whether a surrogate model is used to approximate the objective, at least locally. The first algorithm, the method of local variations, advances through local function evaluations and step size updates. The second algorithm is a Bayesian optimization one that uses Gaussian process as its surrogate model, which is updated with new simulation data.

The organization of this paper is as follows. Section 2 contains a summary of the coupled thermomechanical finite element model. The optimization formulation is given in Section 3. In Section 4, the gradient-based optimization algorithm is described, with derivations of sensitivities. In Section 5, we propose our gradient-free optimization algorithms and discuss algorithmic parameter choices. Numerical examples of the optimization methods are presented in Section 6. Finally, conclusions are included in Section 7.

2 Review of continuum theory and finite element modeling

2.1 Continuum theory

In this paper, it is assumed that the printed body can be adequately modeled as an isotropic and homogeneous thermoelastic continuum undergoing infinitesimal deformation relative to its evolving reference configuration in the presence of large changes in its temperature. The material comprising the body is locally endowed with a Helmholtz free energy function $\psi = \bar{\psi}(\boldsymbol{\epsilon}, \theta)$ per unit volume, where $\boldsymbol{\epsilon}$ and θ are the infinitesimal strain tensor and temperature, respectively.

The local form of linear momentum balance may be expressed as

$$\rho_0 \mathbf{a} = \nabla \cdot \boldsymbol{\sigma} + \rho_0 \mathbf{b} , \tag{1}$$

where ρ_0 is the mass density per unit referential volume, \mathbf{a} is the acceleration, $\boldsymbol{\sigma}$ is the stress tensor of the infinitesimal theory, and \mathbf{b} is the body force per unit mass, while “ ∇ ” denotes the divergence operator relative to the referential coordinates. The balance of angular momentum ensures that the stress tensor $\boldsymbol{\sigma}$ is symmetric. Moreover, the balance of energy takes the form

$$\rho_0 \dot{e} = \rho_0 r - \nabla \cdot \mathbf{q}_0 + \boldsymbol{\sigma} \cdot \dot{\boldsymbol{\epsilon}} , \tag{2}$$

in terms of the internal energy per unit mass e , the heat supply per unit mass r , and the referential heat flux vector $\mathbf{q}_0 = \bar{\mathbf{q}}_0(\boldsymbol{\epsilon}, \theta, \nabla \theta)$.

Upon invoking the Clausius-Duhem inequality, a standard procedure leads to the relations

$$\boldsymbol{\sigma} = \frac{\partial \bar{\psi}(\boldsymbol{\epsilon}, \theta)}{\partial \boldsymbol{\epsilon}} \quad , \quad \mathbf{q}_0 \cdot \nabla \theta \leq 0 \quad , \quad (3)$$

as well as to the reformulation of the energy equation (2) as

$$c \dot{\theta} = -\nabla \cdot \mathbf{q}_0 + \rho_0 r + \theta \mathbf{M} \cdot \dot{\boldsymbol{\epsilon}} \quad , \quad (4)$$

where $c = -\theta \frac{\partial^2 \bar{\psi}(\boldsymbol{\epsilon}, \theta)}{\partial \theta^2}$ is the heat capacity and $\mathbf{M} = \frac{\partial^2 \bar{\psi}(\boldsymbol{\epsilon}, \theta)}{\partial \boldsymbol{\epsilon} \partial \theta}$ is the stress-temperature modulus, see, *e.g.*, [26] for a full derivation.

A Helmholtz free-energy function that can adequately represent materials under infinitesimal deformation and a finite temperature range [76] is chosen according to

$$\bar{\psi}(\boldsymbol{\epsilon}, \theta) = \frac{1}{2} \boldsymbol{\epsilon} \cdot \mathbb{C}(\theta) \boldsymbol{\epsilon} - \kappa(\theta) \ln(1 + \text{tr } \boldsymbol{\epsilon}) \alpha (\theta - \theta_0) + \bar{c} \left(\theta - \theta_0 - \theta \ln \frac{\theta}{\theta_0} \right) \quad , \quad (5)$$

where α is the (constant) coefficient of thermal expansion, θ_0 is the reference temperature, and \bar{c} is the specific heat at the reference temperature. Also, the temperature-dependent isotropic elastic modulus in (5) is expressed as $\mathbb{C}(\theta) = \tilde{f}(\theta) \mathbb{C}_{0,m}$, where $\tilde{f}(\cdot)$ is a smooth and positive function of temperature and $\mathbb{C}_{0,m}$ is the elastic modulus at a given temperature $\theta_{0,m}$, not necessarily equal to the reference temperature θ_0 . Likewise, the temperature-dependent bulk modulus in (5) is approximated as $\kappa(\theta) = \tilde{f}(\theta) \kappa_{0,m}$, with $\kappa_{0,m}$ being the bulk modulus at $\theta_{0,m}$. The temperature function is defined here as

$$\tilde{f}(\theta) = b \left(\frac{\theta}{\theta_{0,m}} \right)^a + b(a-1) + (1-ab) \frac{\theta}{\theta_{0,m}} \quad , \quad (6)$$

where a and b are material constants and $\tilde{f}(\theta_{0,m}) = 1$.

Consistent with the restriction in (3)₂, the heat flux follows the isotropic form of Fourier's law, according to which

$$\mathbf{q}_0 = -k \nabla \theta \quad , \quad (7)$$

where k is the (constant) thermal conductivity coefficient. Also, heat convection is included in the model, such that the flux of heat through the exterior boundary is given by

$$\bar{q} = h(\theta_\infty - \theta) \quad , \quad (8)$$

where h is the (constant) convection coefficient and θ_∞ is the ambient temperature.

In view of the constitutive equation in (5) and upon taking into account (3)₁ and the definitions of the heat capacity c and the stress-temperature modulus \mathbf{M} , it follows that

$$\begin{aligned}
 \boldsymbol{\sigma} &= \tilde{f}(\theta) \left[\mathbb{C}_{0,m} \boldsymbol{\epsilon} - \kappa_{0,m} \alpha \frac{\theta - \theta_0}{1 + \text{tr } \boldsymbol{\epsilon}} \mathbf{I} \right], \\
 \mathbf{M} &= \frac{\partial \tilde{f}(\theta)}{\partial \theta} \mathbb{C}_{0,m} \boldsymbol{\epsilon} - \left[\frac{\partial \tilde{f}(\theta)}{\partial \theta} (\theta - \theta_0) + \tilde{f}(\theta) \right] \kappa_{0,m} \alpha \frac{1}{1 + \text{tr } \boldsymbol{\epsilon}} \mathbf{I}, \\
 c &= -\theta \frac{\partial^2 \tilde{f}(\theta)}{\partial \theta^2} \frac{1}{2} \boldsymbol{\epsilon} \cdot \mathbb{C}_{0,m} \boldsymbol{\epsilon} + \left[\theta \frac{\partial^2 \tilde{f}(\theta)}{\partial \theta^2} (\theta - \theta_0) + \theta \frac{\partial \tilde{f}(\theta)}{\partial \theta} \right] \kappa_{0,m} \alpha \ln(1 + \text{tr } \boldsymbol{\epsilon}) + \bar{c},
 \end{aligned} \tag{9}$$

where \mathbf{I} is the second-order identity tensor.

2.2 Finite element modeling

Let the printed body occupy the region Ω_0 in a reference configuration. The referential boundary $\partial\Omega_0$ of the body is decomposed into Dirichlet parts $\Gamma_{D,0}^u$, $\Gamma_{D,0}^t$ and Neumann parts $\Gamma_{N,0}^u$, $\Gamma_{N,0}^t$ for displacement and temperature, respectively, such that $\overline{\Gamma_{D,0}^u \cup \Gamma_{N,0}^u} = \overline{\Gamma_{D,0}^t \cup \Gamma_{N,0}^t} = \partial\Omega_0$. The weak forms of the balance laws in (1) and (4) are expressed respectively as

$$\begin{aligned}
 \int_{\Omega_0} \boldsymbol{\xi} \cdot \rho_0 \mathbf{a} \, dV + \int_{\Omega_0} \nabla^s \boldsymbol{\xi} \cdot \boldsymbol{\sigma} \, dV &= \int_{\Gamma_{N,0}^u} \boldsymbol{\xi} \cdot \bar{\mathbf{p}} \, dA + \int_{\Omega_0} \boldsymbol{\xi} \cdot \rho_0 \mathbf{b} \, dV, \\
 \int_{\Omega_0} \zeta c \dot{\theta} \, dV - \int_{\Omega_0} \nabla \zeta \cdot \mathbf{q}_0 \, dV &= \int_{\Omega_0} \zeta \rho_0 r \, dV + \int_{\Omega_0} \zeta \theta \mathbf{M} \cdot \dot{\boldsymbol{\epsilon}} \, dV - \int_{\Gamma_{N,0}^t} \zeta \bar{q} \, dA,
 \end{aligned} \tag{10}$$

where ∇^s denotes the symmetric part of the referential gradient, while $\bar{\mathbf{p}}$ and \bar{q} are the imposed traction and flux boundary conditions on $\Gamma_{N,0}^u$ and $\Gamma_{N,0}^t$, respectively. The weak forms are expressed in terms of arbitrary and sufficiently smooth weighting functions $\boldsymbol{\xi}$ for the linear momentum balance and ζ for the energy balance, each satisfying the corresponding homogeneous Dirichlet boundary conditions. The infinitesimal strain tensor is related to the displacement field \mathbf{u} according to $\boldsymbol{\epsilon} = \nabla^s \mathbf{u}$.

Taking into account the arbitrariness of the weighting functions and introducing standard displacement-type finite element piecewise approximations for the dependent variables, their derivatives, and the corresponding weighting functions leads to elemental equations written in matrix form as

$$\begin{aligned}
 [\mathbf{M}_u^e] [\hat{\mathbf{a}}_n^e] + [\mathbf{R}_{u,n}^e] &= [\mathbf{F}_n^e] + \int_{\partial\Omega_0^e \setminus \Gamma_{N,0}^u} [\mathbf{N}_u^e] [\mathbf{p}_n^e] \, dA, \\
 [\mathbf{T}^e] [\hat{\boldsymbol{\theta}}_n^e] + [\mathbf{M}_t^e] [\hat{\boldsymbol{\theta}}_n^e] + [\mathbf{R}_{t,n}^e] &= [\mathbf{Q}_n^e] - \int_{\partial\Omega_0^e \setminus \Gamma_{N,0}^t} [\mathbf{N}_t^e]^T [\mathbf{q}_n^e] \, dA.
 \end{aligned} \tag{11}$$

Here, the subscript “ n ” identifies an algebraic quantity as estimated at time t_n , while the superscript “ e ” refers to the element e . In addition, the overset symbol in $(\hat{\cdot})$ implies that the term under it comprises the set of nodal values associated with the quantity (\cdot) . All the matrices used in (11) are defined in the appendix. Upon neglecting, as is customary, the interelement flux terms, the preceding elemental equations give rise to the global system, expressed as

$$\begin{aligned} [\mathbf{M}_u] [\hat{\mathbf{a}}_n] + [\mathbf{R}_{u,n}] - [\mathbf{F}_n] &= [\mathbf{0}] , \\ [\mathbf{T}] [\hat{\boldsymbol{\theta}}_n] + [\mathbf{M}_t] [\hat{\boldsymbol{\theta}}_n] + [\mathbf{R}_{t,n}] - [\mathbf{Q}_n] &= [\mathbf{0}] , \end{aligned} \quad (12)$$

where any elemental quantity $[(\cdot)^e]$ is assembled into its global counterpart $[(\cdot)]$ by means of a standard assembly operation.

The temporal discretization of the displacement vector $[\hat{\mathbf{u}}]$ and the velocity vector $[\hat{\mathbf{v}}]$ is effected by the standard trapezoidal rule, while the backward Euler rule is employed for the temperature vector $[\hat{\boldsymbol{\theta}}]$. Therefore, given a time interval $(t_{n-1}, t_n]$ of size $\Delta t_{n-1} = t_n - t_{n-1}$,

$$\begin{aligned} [\hat{\mathbf{u}}_n] &= [\hat{\mathbf{u}}_{n-1}] + [\hat{\mathbf{v}}_{n-1}] \Delta t_{n-1} + \frac{1}{4} \{[\hat{\mathbf{a}}_{n-1}] + [\hat{\mathbf{a}}_n]\} \Delta t_{n-1}^2 , \\ [\hat{\mathbf{v}}_n] &= [\hat{\mathbf{v}}_{n-1}] + \frac{1}{2} \{[\hat{\mathbf{a}}_{n-1}] + [\hat{\mathbf{a}}_n]\} \Delta t_{n-1} , \\ [\hat{\boldsymbol{\theta}}_n] &= [\hat{\boldsymbol{\theta}}_{n-1}] + [\hat{\boldsymbol{\theta}}_n] \Delta t_{n-1} . \end{aligned} \quad (13)$$

Taking into account the constitutive laws (7–9) and the time-stepping rules in (13), the system of linear algebraic equations at the k -th Newton-Raphson iteration in the time interval $(t_{n-1}, t_n]$ can be written in matrix form as

$$\begin{aligned} [\mathbf{M}_u] [\hat{\mathbf{a}}_n^{(k)}] + [\mathbf{R}_{u,n}^{(k)}] - [\mathbf{F}_n] \\ + [\mathbf{K}_{u,n}^{(k)}] [\Delta \hat{\mathbf{u}}_n^{(k)}] + [\mathbf{K}_{t,n}^{(k)}] [\Delta \hat{\boldsymbol{\theta}}_n^{(k)}] &= [\mathbf{0}] , \\ [\mathbf{T}] [\hat{\boldsymbol{\theta}}_n^{(k)}] + [\mathbf{M}_t] [\hat{\boldsymbol{\theta}}_n^{(k)}] + [\mathbf{R}_{t,n}^{(k)}] - [\mathbf{Q}_n] \\ + [\mathbf{A}_{u,n}^{(k)}] [\Delta \hat{\mathbf{u}}_n^{(k)}] + [\mathbf{A}_{t,n}^{(k)}] [\Delta \hat{\boldsymbol{\theta}}_n^{(k)}] &= [\mathbf{0}] , \end{aligned} \quad (14)$$

where $\Delta(\cdot)_n$ is the change of the variable (\cdot) in $(t_{n-1}, t_n]$. Expressions for the tangent matrices $[\mathbf{K}_{u,n}^{(k)}]$, $[\mathbf{K}_{t,n}^{(k)}]$, $[\mathbf{A}_{u,n}^{(k)}]$, and $[\mathbf{A}_{t,n}^{(k)}]$ in (14) are provided in the appendix. The global displacement and temperature vectors are updated according to

$$[\hat{\mathbf{u}}_n^{(k+1)}] = [\hat{\mathbf{u}}_n^{(k)}] + [\Delta \hat{\mathbf{u}}_n^{(k)}] , \quad [\hat{\boldsymbol{\theta}}_n^{(k+1)}] = [\hat{\boldsymbol{\theta}}_n^{(k)}] + [\Delta \hat{\boldsymbol{\theta}}_n^{(k)}] , \quad (15)$$

until convergence is attained in a predefined stopping criterion and a prescribed tolerance.

To accommodate new nodes and elements generated when material is deposited on the boundary of the existing body, each node is assigned an initial displacement and temperature. These “history” variables ensure zero initial stress and strain. To this end, the displacement history values are subtracted from the nodal displacement values when computing the strain and stress at a typical integration point. Likewise, the temperature history value represents the reference temperature θ_0 in (9) of an element when it is first created, computed as the average of the nodal temperature of the element.

For printed objects that have curved boundaries, our simulation relies on a slicing algorithm to determine how the curves are approximated and printed. The choice of the slicing algorithm is not a focus of this study. For the one that is used in our finite element model, the reader can find it in [26]. In general however, curved boundaries require the use of partial elements that involve hanging nodes. The reference coordinates of the hanging nodes are determined by the slicing algorithm while their displacement and temperature are solved together with the rest of the displacement and temperature field. To do so, additional conditions need to be imposed if a hanging node lies on an existing edge. When such a node is created, a ratio of its coordinates and those of two nodes that define this existing edge can be computed. This ratio is then maintained when computing for the displacement and temperature of the hanging node, so that it would remain at the same relative position of the edge throughout the simulation. Full details on the implementation of history variables and hanging nodes can be found in [26].

3 Optimization problem formulation

Let $f(\mathbf{u}, \boldsymbol{\theta}; \mathbf{y}, t)$ be the objective function of the design optimization problem, where $\mathbf{y} \in \mathbb{R}^d$ represents the vector set of d design variables, *i.e.*, process parameters such as chamber temperature and layer thickness. The continuum-level optimization problem can be expressed as

$$\begin{aligned} & \underset{\mathbf{y} \in \mathbb{R}^d}{\text{minimize}} && f(\mathbf{u}, \boldsymbol{\theta}; \mathbf{y}, t) , \\ & \text{subject to} && \mathbf{r}(\mathbf{u}, \boldsymbol{\theta}; \mathbf{y}, t) = \mathbf{0} , \quad c_i(\mathbf{y}) \leq 0 , \quad i = 1, \dots, m . \end{aligned} \tag{16}$$

Here, \mathbf{r} comprises the balance laws in (10) (before the finite element approximation), while $c_i(\cdot)$, $i = 1, \dots, m$, are inequality constraint functions on the design variables.

In this paper, the objective function is chosen to express the deviation of the part’s actual shape from the desired shape. Such deviation, or shape error, may pose significant

challenges in AM [77]. In the two-dimensional case, given a fixed reference configuration, shape error may be defined as

$$f(\mathbf{u}, \boldsymbol{\theta}; \mathbf{y}, t) = \frac{\left[\int_{\Gamma_S^t} (d(\mathbf{X}, \mathbf{u}) - \bar{d}(\mathbf{X}))^2 dl \right]^{\frac{1}{2}}}{L_c \left(\int_{\Gamma_S^t} dl \right)^{\frac{1}{2}}}, \quad (17)$$

where \mathbf{X} represent the placement of the boundary points on the (necessarily time-dependent) surface of interest Γ_S^t in the designed geometry under no deformation. Also, $d(\mathbf{X}, \mathbf{u}) - \bar{d}(\mathbf{X})$ is a problem-dependent scalar measure of the difference of the printed position d from the designed position \bar{d} on Γ_S^t , while L_c is a representative length of the part intended to render f dimensionless. As seen from (17), the objective function depends explicitly on \mathbf{u} alone. Upon finite element discretization, the objective function f is measured on one-dimensional element edges and can be evaluated numerically using Gaussian quadrature. The discrete counterpart f_h of the objective function for linear elements is given by

$$f_h(\hat{\mathbf{u}}, \hat{\boldsymbol{\theta}}; \mathbf{y}, t) = \frac{\left[\sum_{i=1}^p \sum_{j=1}^l (d(\mathbf{X}_j, \mathbf{u}_j) - \bar{d}(\mathbf{X}_j))^2 w_j \frac{\Delta l_i}{2} \right]^{\frac{1}{2}}}{L_c \left(\sum_{i=1}^p \Delta l_i \right)^{\frac{1}{2}}}, \quad (18)$$

where p is the number of discretized edges of interest, Δl_i is the length of the i -th edge, l is the number of quadrature points per edge, and w_j is the weight of the j -th quadrature point. The values of $\mathbf{X}_j, \mathbf{u}_j$ at quadrature points are evaluated using \mathbf{X} and the nodal displacement $\hat{\mathbf{u}}$. The precise definition of the position deviation $d(\mathbf{u}) - \bar{d}$ is specified in Section 6 for each example. Implicit in the preceding definitions of f and f_h is that d induces a bijection between the designed to the printed surface regardless of the value of the displacement \mathbf{u} , see Figure 1.

Depending on the nature of \mathbf{y} , the optimization problem (16) may require the use of substantially different algorithms. For example, some process parameters, such as chamber temperature, vary continuously. Hence, the objective function f_h may be considered implicitly differentiable in them. This would enable the application of well-established gradient-based optimization algorithms. On the other hand, parameters such as layer thickness, which is mandated by the (integer) number of layers for a given specimen size, are discrete and, therefore, non-differentiable. For optimization in such variables, a gradient-free algorithm would be appropriate.

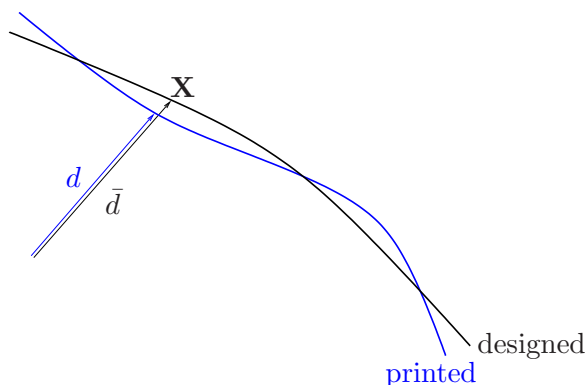


Figure 1: Schematic of the distance functions d and \bar{d}

4 Gradient-descent method with line search

For gradient-based optimization methods, the derivatives of the discretized objective f_h from (18) with respect to design variables \mathbf{y} must be known or estimated. Let N be the total number of discrete time steps in the analysis. For simplicity, denote the combined system of fully discretized PDEs at time $t_n, 1 \leq n \leq N$, as \mathbf{r}_n^h , where the superscript h is included to emphasize the discrete vector form of the variables. It follows that the discretized form of the PDE constraint in (16) can be expressed as

$$\mathbf{r}_n^h \left(\hat{\mathbf{u}}_n^h, \hat{\mathbf{u}}_{n-1}^h, \hat{\mathbf{v}}_{n-1}^h, \hat{\boldsymbol{\theta}}_n^h, \hat{\boldsymbol{\theta}}_{n-1}^h, \hat{\mathbf{u}}_n^{his}, \hat{\boldsymbol{\theta}}_n^{his}; \mathbf{y}, t_n \right) = \mathbf{0}, \quad (19)$$

in view of the single-step time integration rules in (15). As noted in Section 2, the history variables $\mathbf{u}_n^{his}, \boldsymbol{\theta}_n^{his}$ represent the displacement and temperature field at each new node and element when they are added at their respective time step. Thus, they are also discrete in form and full details on their precise definition may be found in [26]. In addition, it is assumed that any inequality constraints $c_i(\cdot)$ on \mathbf{y} can be included by requiring that $\mathbf{y} \in \mathfrak{C}$, where $\mathfrak{C} \subset \mathbb{R}^m$ is a suitably defined convex and compact set.

The solver-consistent discretized form of (16) is now expressed as

$$\begin{aligned} & \underset{\mathbf{y} \in \mathfrak{C}}{\text{minimize}} && f_h \left(\hat{\mathbf{u}}_N^h, \hat{\boldsymbol{\theta}}_N^h; \mathbf{y}, t_N \right) \\ & \text{subject to} && \mathbf{r}_n^h \left(\hat{\mathbf{u}}_n^h, \hat{\mathbf{u}}_{n-1}^h, \hat{\mathbf{v}}_{n-1}^h, \hat{\boldsymbol{\theta}}_n^h, \hat{\boldsymbol{\theta}}_{n-1}^h, \hat{\mathbf{u}}_n^{his}, \hat{\boldsymbol{\theta}}_n^{his}; \mathbf{y}, t_n \right) = \mathbf{0}, \quad n = 1, 2, \dots, N. \end{aligned} \quad (20)$$

The preceding discrete optimization problem reflects the fact that only the end-state is of consequence in the design.

Consider the reduced-space formulation, in which \mathbf{u}_N^h and $\boldsymbol{\theta}_N^h$ are regarded as implicit functions of \mathbf{y} at time t_N and also let N be independent of \mathbf{y} . Then, by chain rule, the

gradient of f_h with respect to \mathbf{y} is

$$\frac{df_h}{d\mathbf{y}} = \frac{\partial f_h}{\partial \hat{\mathbf{u}}_N^h} \frac{\partial \hat{\mathbf{u}}_N^h}{\partial \mathbf{y}} + \frac{\partial f_h}{\partial \hat{\boldsymbol{\theta}}_N^h} \frac{\partial \hat{\boldsymbol{\theta}}_N^h}{\partial \mathbf{y}} + \frac{\partial f_h}{\partial \mathbf{y}}. \quad (21)$$

Each term on the right-hand-side of (21) is derived next. First, note that, owing to the explicit dependence of f_h on \mathbf{y} , $\hat{\mathbf{u}}_N^h$, and $\hat{\boldsymbol{\theta}}_N^h$, the terms $\frac{\partial f_h}{\partial \mathbf{y}}$, $\frac{\partial f_h}{\partial \hat{\mathbf{u}}_N^h}$, and $\frac{\partial f_h}{\partial \hat{\boldsymbol{\theta}}_N^h}$ can be computed directly by differentiating the function f_h . Of course, given the specific form of f_h in (18), the only non-zero such term here is $\frac{\partial f_h}{\partial \hat{\mathbf{u}}_N^h}$. On the other hand, the state sensitivities $\frac{\partial \hat{\mathbf{u}}_N^h}{\partial \mathbf{y}}$ and $\frac{\partial \hat{\boldsymbol{\theta}}_N^h}{\partial \mathbf{y}}$ at t_N are dependent on those of the previous time steps, that is, $\frac{\partial \hat{\mathbf{u}}_n^h}{\partial \mathbf{y}}$ and $\frac{\partial \hat{\boldsymbol{\theta}}_n^h}{\partial \mathbf{y}}$, for $n = 1, \dots, N - 1$. Due to the small total number of optimization variables, a pure primal approach is adopted here to obtain the sensitivities. To this end, upon differentiation of both sides of Equation (19) with respect to \mathbf{y} , it follows that

$$\begin{aligned} \frac{\partial \mathbf{r}_n^h}{\partial \hat{\mathbf{u}}_n^h} \frac{\partial \hat{\mathbf{u}}_n^h}{\partial \mathbf{y}} + \frac{\partial \mathbf{r}_n^h}{\partial \hat{\mathbf{u}}_{n-1}^h} \frac{\partial \hat{\mathbf{u}}_{n-1}^h}{\partial \mathbf{y}} + \frac{\partial \mathbf{r}_n^h}{\partial \hat{\mathbf{v}}_{n-1}^h} \frac{\partial \hat{\mathbf{v}}_{n-1}^h}{\partial \mathbf{y}} + \frac{\partial \mathbf{r}_n^h}{\partial \hat{\boldsymbol{\theta}}_n^h} \frac{\partial \hat{\boldsymbol{\theta}}_n^h}{\partial \mathbf{y}} + \frac{\partial \mathbf{r}_n^h}{\partial \hat{\boldsymbol{\theta}}_{n-1}^h} \frac{\partial \hat{\boldsymbol{\theta}}_{n-1}^h}{\partial \mathbf{y}} \\ + \frac{\partial \mathbf{r}_n^h}{\partial \hat{\mathbf{u}}_n^{his}} \frac{\partial \hat{\mathbf{u}}_n^{his}}{\partial \mathbf{y}} + \frac{\partial \mathbf{r}_n^h}{\partial \hat{\boldsymbol{\theta}}_n^{his}} \frac{\partial \hat{\boldsymbol{\theta}}_n^{his}}{\partial \mathbf{y}} + \frac{\partial \mathbf{r}_n^h}{\partial \mathbf{y}} = \mathbf{0}. \quad (22) \end{aligned}$$

The state sensitivities $\frac{\partial \hat{\mathbf{u}}_n^h}{\partial \mathbf{y}}$ and $\frac{\partial \hat{\boldsymbol{\theta}}_n^h}{\partial \mathbf{y}}$ at time t_n are obtained from (22), in terms of the rest of the (known) terms in the equation, including the state sensitivities at t_{n-1} . The initial conditions for these sensitivities are set to zero, since the initial displacement and temperature fields are prescribed.

It is important to note here that use of the Newton-Raphson method for the solution to $\mathbf{r}_n^h = \mathbf{0}$ requires the calculation of the ‘‘stiffness’’ terms $\frac{\partial \mathbf{r}_n^h}{\partial \hat{\mathbf{u}}_n^h}$ and $\frac{\partial \mathbf{r}_n^h}{\partial \hat{\boldsymbol{\theta}}_n^h}$. Therefore, these two terms (which are derived in the appendix) are already available for the sensitivity calculations. Furthermore, the terms $\frac{\partial \mathbf{r}_n^h}{\partial \hat{\mathbf{u}}_{n-1}^h}$, $\frac{\partial \mathbf{r}_n^h}{\partial \hat{\mathbf{v}}_{n-1}^h}$, and $\frac{\partial \mathbf{r}_n^h}{\partial \hat{\boldsymbol{\theta}}_{n-1}^h}$, which appear in (22), can be readily obtained by substituting the time-stepping formulae (13) into (12) and taking the derivatives of the discrete governing equations comprising \mathbf{r}_n^h with respect to $\mathbf{u}_{n-1}^h, \boldsymbol{\theta}_{n-1}^h, \mathbf{v}_{n-1}^h$. Again, explicit expressions for these terms may be found in the appendix.

Based on the implementation of the history variables $\hat{\mathbf{u}}_n^{his}$ and $\hat{\boldsymbol{\theta}}_n^{his}$, it is straightforward to compute the corresponding sensitivities $\frac{\partial \hat{\mathbf{u}}_n^{his}}{\partial \mathbf{y}}$ and $\frac{\partial \hat{\boldsymbol{\theta}}_n^{his}}{\partial \mathbf{y}}$ in Equation (22) at the element level and then assemble into their global counterparts (for details see, again, [26]). Since the history variables are simply the displacement and temperature of a node and an element, respectively, at the time they are created, they remain constant throughout the simulation. Thus, the displacement history variable sensitivity $\frac{\partial \hat{\mathbf{u}}_n^{his,e}}{\partial \mathbf{y}}$ is simply the displacement sensitivity at the time of the creation of a node, and the temperature history

sensitivity $\frac{\partial \hat{\theta}_n^{his,e}}{\partial \mathbf{y}}$ is the average of the nodal temperature sensitivity of an element. These sensitivities are stored for subsequent use. The same applies to the derivative terms $\frac{\partial \mathbf{r}_n^h}{\partial \hat{\mathbf{u}}_n^{his}}$ and $\frac{\partial \mathbf{r}_n^h}{\partial \hat{\theta}_n^{his}}$, which are derived in the appendix.

At each time t_n , the state sensitivities at t_{n-1} are stored and used in the solution of (22). The last remaining term in (22), $\frac{\partial \mathbf{r}_n^h}{\partial \mathbf{y}}$, can be explicitly computed once the optimization variable \mathbf{y} is defined. With all the necessary terms now available, Equation (22) is solved for $\frac{\partial \hat{\mathbf{u}}_n^h}{\partial \mathbf{y}}$ and $\frac{\partial \hat{\theta}_n^h}{\partial \mathbf{y}}$, subject to the initial sensitivities (taken here to be zero).

All the sensitivities computed here analytically have been tested against second-order accurate centered-finite difference approximation to ensure the faultlessness of the derivations.

Given the initial displacement vector $\hat{\mathbf{u}}_0^h$, temperature vector $\hat{\theta}_0^h$ and design variable vector \mathbf{y}_0 , it is now possible to compute the gradient (21). The optimization problem (20) can be recast in reduced-space as

$$\underset{\mathbf{y} \in \mathcal{C}}{\text{minimize}} \quad f_h(\mathbf{u}_0, \theta_0, \mathbf{y}, t_N) . \quad (23)$$

For relatively small dimension of \mathbf{y} , many well-established nonlinear optimization methods may be used to solve this problem. Here, a projected gradient-descent method with line search is employed, as described in Algorithm 1. The initial sensitivities $\frac{\partial \hat{\mathbf{u}}_0}{\partial \mathbf{y}}$ and $\frac{\partial \hat{\theta}_0}{\partial \mathbf{y}}$ are set to 0 as they do not depend on \mathbf{y} at the starting time t_0 .

Algorithm 1: Projected gradient descent with line search

- 1 Let $\alpha_0 = 1$, $\rho \in (0, 1)$, $\eta \in (0, 1)$
 - 2 **for** $k = 0, 1, 2, \dots$ **do**
 - 3 Perform the finite element simulation. Compute sensitivities and the gradient in (21).
 - 4 Let $\mathbf{p}_k = -\frac{df_h(\mathbf{y}_k)}{d\mathbf{y}_k} / \|\frac{df_h(\mathbf{y}_k)}{d\mathbf{y}_k}\|$.
 - 5 Set $\alpha_k \leftarrow \alpha_0$.
 - 6 **while** $f_h(\mathbf{y}_k + \alpha_k \mathbf{p}_k) > f_h(\mathbf{y}_k) + \eta \alpha_k \left[\frac{df_h(\mathbf{y}_k)}{d\mathbf{y}_k} \right]^T \mathbf{p}_k$ **do**
 - 7 $\alpha_k \leftarrow \rho \alpha_k$
 - 8 $\mathbf{y}_{k+1} = \mathbf{y}_k + \alpha_k \mathbf{p}_k$
 - 9 Project \mathbf{y}_{k+1} onto \mathcal{C} .
-

In this algorithm, η and ρ are user-specified constants, while the scalar α_k is the length of the line-search step. It is worth pointing out that the line-search step could be compu-

tationally expensive as f_h needs to be evaluated each time α_k is updated. The projection step for a general convex and compact \mathfrak{C} typically involves solving a minimum-distance problem. However, in the case of bound constraints, one is only required to force \mathbf{y} to stay inside the bounds. For more complicated constraints which are nonlinear in \mathbf{y} , this algorithm would not suffice. For the purposes of this work, Algorithm 1 is implemented in both C++ and Python.

5 Gradient-free Optimization Methods

Two optimization algorithms are presented in this section for the solution of (16) and (23) that do not require sensitivities and rely only on objective function evaluations. The first is a local search algorithm that advances by comparing objective values at neighboring points in the design space. Owing to parallel computing, this algorithm can quickly yield reasonable results and is easy to implement. The second is a Bayesian optimization algorithm, where a surrogate model for the objective is built using samples. The solution to the optimization problem is updated based on the prediction of the surrogate model. Algorithms of this type have received significant attention in the past decade and have been shown to efficiently generate global optimal result [78].

5.1 Method of local variations

This is a version of the method of local variations proposed by Polak [79] and is shown in Algorithm 2. It is used here to solve the reduced formulation (23) of the design optimization problem. The algorithm starts with a guess in the optimization variable space and takes a series of steps towards an optimal solution by constantly comparing neighborhood objective values and adjusting step sizes. Multiple starting points can be used to improve the results, as the algorithm can be shown to reach a local minimum if the objective is continuously differentiable [79]. Denote the initial step size as τ_0 and start with $\mathbf{y}_0 \in \mathfrak{C} \subset \mathbb{R}^d$. The minimum step size is controlled by vector τ_{min} . At each iteration k , the algorithm centers around the current point \mathbf{y}_k in the optimization space and runs $2d$ simulations on neighboring points, with the neighboring points selected by the step size τ and directions \mathbf{d}_j , $j = 1, \dots, 2d$. If neighboring points produce smaller values of the objective, the point that produces the smallest value is selected to be the next iteration point. If no such point can be found, the current step size τ_k is reduced and simulation at new neighboring points are run until the step size of each variable becomes smaller than each component of

Algorithm 2: Method of local variations

- 1 Select a $\mathbf{y}_0 \in \mathbb{R}^d$ such that $\mathbf{y}_0 \in \mathcal{C}$ is feasible. Select a $\tau_0 > 0$.
 - 2 Set $k = 0$, and compute $f_h(\mathbf{y}_0)$. Let $f_{min} = f_h(\mathbf{y}_0)$; **while** $\tau_k > \tau_{min}$ **do**
 - 3 Set $f_{min} = f_h(\mathbf{y}_k)$ and $\mathbf{d}_{min} = \mathbf{0}$.
 - 4 **for** $j = 1, \dots, 2n$ **do**
 - 5 Check if $\mathbf{z}_k^j = \mathbf{y}_k + (\tau_k)_{j/2} \mathbf{d}_j \in \mathcal{C}$. Project it onto \mathcal{C} if not so that $\mathbf{z}_k^j \in \mathcal{C}$.
 - 6 Compute $f_h(\mathbf{z}_k^j)$.
 - 7 **if** $f_h(\mathbf{z}_k^j) < f_{min}$ **then**
 - 8 $f_{min} = f_h(\mathbf{z}_k^j)$.
 - 9 $\mathbf{d}_{min} = \mathbf{z}_k^j - \mathbf{y}_k$.
 - 10 $\mathbf{y}_{k+1} = \mathbf{y}_k + \mathbf{d}_{min}$.
 - 11 **if** $f_{min} < f_h(\mathbf{y}_k)$ **then**
 - 12 $\tau_{k+1} = \tau_k$, $k = k + 1$.
 - 13 **else**
 - 14 Reduce the step size via $(\tau_{k+1})_j = (\tau_k)_j / 2$ or $(\tau_{k+1})_j = (\tau_k)_j - 1$ for
 $j = 1, \dots, n$. Set $k = k + 1$.
-

τ_{min} . The quantity \mathbf{d}_j represents the increasing and decreasing search direction for each component of \mathbf{y} . In Algorithm 2, the default optimization variable is continuous, and thus the step size can be repeatedly reduced by half. However, the algorithm can be readily adapted to discrete optimization variables. Specifically, for an integer parameter such as the number of deposition layers, one may reduce the step size $\|\tau_k \mathbf{d}_j\|$ by 1. The algorithm enforces the simple constraints at step 6 so that all points evaluated are feasible.

5.2 Bayesian optimization method

A Bayesian optimization algorithm [80] is alternatively employed to solve Problem (23). This is a “black-box” sequential surrogate-based optimization method, where the objective and the associated PDEs are represented by a surrogate model and, therefore, no sensitivity calculations are necessary. The surrogate model is typically a random function with a prior that is constructed and updated based on the samples (data points) collected. Then, a posterior distribution is formed using the sequentially updated prior so that a prediction of the objective at a given point can be made [78, 81]. In addition, an acquisition function is used to determine where to sample next. This function strikes a balance between

exploitation and exploration, which correspond to an improved objective value and lower uncertainty, respectively.

A sample in the Bayesian optimization process is the individual finite element simulation and its objective value given the process parameters \mathbf{y} . The well-tested Gaussian process (GP) is chosen for the surrogate model, while the expected improvement acquisition function is adopted. Given the sample points, GP assumes a multivariate jointly-Gaussian distribution between \mathbf{y} and the objective function f_h :

$$\begin{bmatrix} f_h(\mathbf{y}_1) \\ \vdots \\ f_h(\mathbf{y}_N) \end{bmatrix} \sim \mathcal{N} \left(\begin{bmatrix} m(\mathbf{y}_1) \\ \vdots \\ m(\mathbf{y}_N) \end{bmatrix}, \begin{bmatrix} k(\mathbf{y}_1, \mathbf{y}_1) \dots k(\mathbf{y}_1, \mathbf{y}_N) \\ \vdots \\ k(\mathbf{y}_N, \mathbf{y}_1) \dots k(\mathbf{y}_N, \mathbf{y}_N) \end{bmatrix} \right). \quad (24)$$

Here, \mathcal{N} is the normal distribution, $\mathbf{y}_1, \dots, \mathbf{y}_N$ are the samples, $m(\cdot) : \mathbb{R}^N \rightarrow \mathbb{R}$ is the mean function, and $k(\cdot, \cdot) : \mathbb{R}^N \times \mathbb{R}^N \rightarrow \mathbb{R}$ is the covariance function. Then, the posterior probability distribution of a new \mathbf{y} can be inferred using Bayes' rule [80],

$$\begin{aligned} f_h(\mathbf{y}) | \mathbf{y}, \mathbf{y}_{1:N}, f_h(\mathbf{y}_{1:N}) &\sim \mathcal{N}(\mu(\mathbf{y}), \sigma^2(\mathbf{y})), \\ \mu(\mathbf{y}) &= k(\mathbf{y}, \mathbf{y}_{1:N})k(\mathbf{y}_{1:N}, \mathbf{y}_{1:N})^{-1} (f_h(\mathbf{y}_{1:N}) - m(\mathbf{y}_{1:N})) + m(\mathbf{y}_{1:N}), \\ \sigma^2(\mathbf{y}) &= k(\mathbf{y}, \mathbf{y}) - k(\mathbf{y}, \mathbf{y}_{1:N})k(\mathbf{y}_{1:N}, \mathbf{y}_{1:N})^{-1} \sigma(\mathbf{y}_{1:N}, \mathbf{y}), \end{aligned} \quad (25)$$

where the vector $\mathbf{y}_{1:N}$ is the notation for $\mathbf{y}_1, \dots, \mathbf{y}_N$ and $k(\mathbf{y}_{1:N}, \mathbf{y}_{1:N}) = [k(\mathbf{y}_1, \dots, k(\mathbf{y}_N); \dots; k(\mathbf{y}_N, \mathbf{y}_1), \dots, k(\mathbf{y}_N, \mathbf{y}_N)]$. The function $\mu(\cdot)$ and $\sigma^2(\cdot)$ are referred to as the posterior mean and variance, respectively. The mean function $m(\cdot)$ is often simply a constant function. The covariance functions, or kernels, of the GP is critical to an accurate surrogate model. The Squared Exponential Covariance Function [82] or power exponential kernel is adopted in this paper. The definition of the covariance function is

$$k(\mathbf{y}, \mathbf{y}'; \theta) = \exp \left(-\frac{\|\mathbf{y} - \mathbf{y}'\|^2}{\theta^2} \right), \quad (26)$$

where θ denotes the hyper-parameters of the kernel. The GP model's hyper-parameters are optimized during the regression by maximizing the log-marginal-likelihood with the BFGS method [83]. The expected improvement acquisition function can be written as

$$EI(\mathbf{y}) = \begin{cases} (\mu(\mathbf{y}) - f_h(\mathbf{y}^+) - \xi)\Phi(Z) + \sigma(\mathbf{y})\phi(Z), & \text{if } \sigma(\mathbf{y}) > 0 \\ 0, & \text{if } \sigma(\mathbf{y}) = 0 \end{cases}, \quad (27)$$

where

$$Z = \begin{cases} \frac{\mu(\mathbf{y}) - f_h(\mathbf{y}^+) - \xi}{\sigma(\mathbf{y})}, & \text{if } \sigma(\mathbf{y}) > 0 \\ 0, & \text{if } \sigma(\mathbf{y}) = 0 \end{cases}, \quad (28)$$

and $\mathbf{y}^+ = \operatorname{argmax}_{\mathbf{y}_i \in \mathbf{y}_{1:N}} f_h(\mathbf{y}_i)$ of all N current samples [82]. The trade-off parameter $\xi > 0$ controls the balance between exploration and exploitation. At an input \mathbf{y} , the mean value predicted by the surrogate is $\mu(\mathbf{y})$ and the variance is $\sigma(\mathbf{y})$. The functions ϕ and Φ are the probability density function (PDF) and cumulative distribution function (CDF) of the standard normal distribution, respectively. In order to find the maximal point of the acquisition function, which would be the next sample point, optimization algorithms including L-BFGS or random search can be used. The Bayesian optimization (BO) algorithm applied to (23) is given in Algorithm 3. An example convergence measure that allows the algorithm to terminate is if consecutive optimization iterations produce optimal point and optimal value within a tolerance range, using the updated Gaussian process surrogate model that includes the latest samples.

Algorithm 3: Bayesian optimization with Gaussian process

- 1 Choose initial sampling data \mathbf{y}_0 .
 - 2 Train the Gaussian process model with \mathbf{y}_0 .
 - 3 **for** $k = 1, 2, \dots$ **do**
 - 4 Evaluate the acquisition function using sample points $\{\mathbf{y}_0, \dots, \mathbf{y}_{k-1}\}$ and find
 $\mathbf{y}_k = \operatorname{argmax}_{\mathbf{y}} EI(\mathbf{y})$.
 - 5 Run finite element simulation with design variables \mathbf{y}_k .
 - 6 Compute the objective $f_h(\mathbf{y}_k)$ based on the simulation result.
 - 7 Retrain the GP surrogate model with the addition of the new sample \mathbf{y}_k and
 $f_h(\mathbf{y}_k)$.
 - 8 Solve the optimization problem with the updated surrogate model.
 - 9 Evaluate convergence measure. Exit if satisfied.
-

Algorithm 3 is implemented in Python and C++ with scikit-learn machine learning library [84, 85] and uses standardscaler preprocessing which reduces the mean of the objective data to 0 and scales them to unit variance. We note that Bayesian optimization is typically implemented as an maximization algorithm. Therefore, we take the negative value of the objective as the actual output to the implementation.

6 Numerical experiments

In this section, Algorithms 1, 2 and 3 are applied to two-dimensional AM optimization problems in conjunction with the material model and the finite element method described in Section 2. All finite element simulations employ standard 4-node rectangular elements with 3×3 Gaussian quadrature, see [26] for full details. In particular, two numerical examples are simulated and the process parameters \mathbf{y} being optimized comprise printing speed, layer thickness and convection coefficient.

6.1 Two-dimensional wall after heat dissipation

The first example involves a two-dimensional rectangular wall with width of $20mm$ and height of $10mm$ in its reference configuration. It is discretized by $n_x = 40$ elements along the horizontal direction and $n_y = 30$ elements in the vertical direction. The bottom side is subjected to Dirichlet boundary conditions with zero displacement and constant temperature at the ambient value of $315K$. The other three sides are traction-free and under convection heat transfer conditions with $\theta_\infty = 315K$. The initial temperature of the deposited material is set to $500K$. To help enforce the boundary conditions, an initial material layer is placed at the base of the body with its bottom nodes subjected to the Dirichlet boundary conditions described above. Each time step corresponds to the time it takes to print one full element. The time interval between the completion of one layer and the initiation of the next one is set to one-half the time needed to print a full layer. The simulation terminates $240s$ after printing is completed to allow the wall to cool down close to the ambient temperature so that the shape error of different process parameters can be measured in a comparable manner.

For this problem, the shape error is measured only at the top edges of the wall, which defines Γ_S^t in (17). The local shape error $d(\mathbf{X}, \mathbf{u}) - \bar{d}(\mathbf{X})$ in (17) is defined as the difference between the y -coordinate of a point in the deformed configuration and its designed height at the same x -coordinate of the reference configuration, as in Figure 2. The approximation (18) of the surface integral, *i.e.*, the objective, is effected using 3-point Gaussian quadrature per element edge. Also, the critical length L_c is chosen to be the height of the wall. The projected gradient-descent Algorithm 1 is applied to the optimization of convection coefficient h , which can be controlled through mechanisms such as the cooling fan speed in the printing chamber. The algorithmic parameters are set to $\alpha_0 = 1$, $\rho = 0.5$, and $\eta = 0.1$. The time-step size for printing a full element is set to $0.006s$, equivalent to a

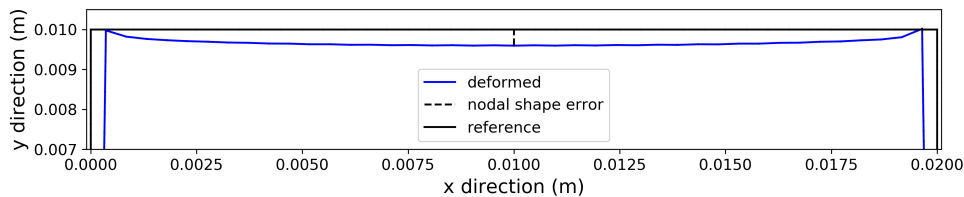


Figure 2: Measurement of shape error for two-dimensional wall with deformation magnified five times for visual clarity (the reference edges in black have zero shape error, while the deformed ones in blue deviate from the designed height due to the thermomechanical response of the material)

printing speed of approximately 83mm/s , within the range of FDM. The number of layers is fixed at 40. The bound constraints on h are set according to $h \in [30, 55]W/m^2K$. Clearly, the optimization space here is one-dimensional and the gradient $\frac{df_h}{dy}$ can be computed as described in Section 4 and the appendix. The initial value h_0 is set to $40W/m^2K$.

A plot depicting the results of the optimization is shown in Figure 3. Taking a closer look at the initial step where $h = 40W/m^2K$, the objective function is $f_h(40) = 0.0233137$, while the gradient value is $\frac{df_h}{dh}(40) = -9.4 \times 10^{-6}$. Upon conducting another full simulation for which $f_h(41) = 0.0233041$, the step-size $\alpha_k = 1$ satisfies the line search condition. Hence, the actual step length is 1 and the next convection coefficient in the iteration is $h = 41W/m^2K$. In a similar manner, the algorithm eventually reaches the optimal value $h = 55W/m^2K$ at the boundary of the feasible space. The dotted line in Figure 3 illustrates the monotonically decreasing dependence of f_h on h , which is physically plausible.

Next, the gradient-free optimization Algorithm 2 and 3 are applied to two important process parameters. These are printing speed, represented by time-step size δt needed to print one element, and layer thickness Δy . Clearly, for a given specimen width and number of elements in the horizontal direction, the printing speed is inversely proportional to δt . Both process parameters present challenges when using gradient-based optimization algorithms. Layer thickness is a discrete parameter as it is dictated by object height and the number of layers. Hence, the objective is not differentiable with respect to it. Likewise, printing speed is tied to the time-step size Δt_n of the finite element formulation in (13), and therefore requires additional effort for sensitivity calculation. Consequently, gradient-free optimization methods present an attractive alternative for these two design parameters.

The bound constraints for the process parameters are set here to

$$\begin{aligned} 0.20\text{mm} &\leq \Delta y \leq 0.33\text{mm}, \\ 0.005\text{s} &\leq \delta t \leq 0.01\text{s}. \end{aligned} \tag{29}$$

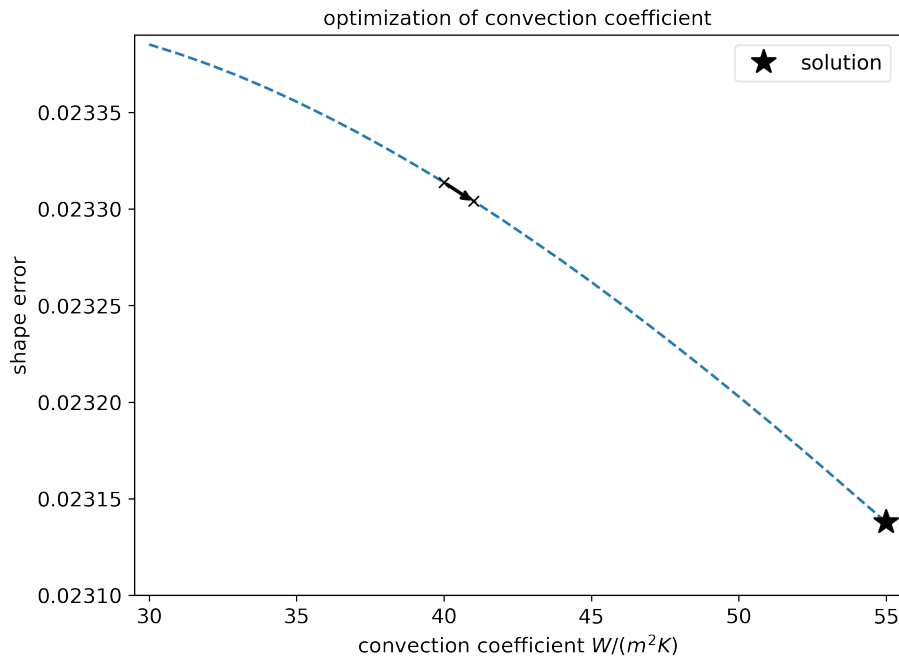


Figure 3: Two-dimensional wall: Optimization of convection coefficient

These reflect a realistic range for each parameter. Also, the convection coefficient h is fixed at $40W/m^2K$.

For the method of local variations, the optimization space is a well-defined two-dimensional rectangle, as shown in Figure 4. The initial optimization step-size τ_0 is set to 4 for number of layers and $0.001s$ for the printing time step. The starting point in the parameter space is set to $\Delta y = 0.25mm$, which corresponds to 40 layers, and $\delta t = 0.0075s$, which translates to a printing speed of $v = 76.2mm/s$. The final step size τ_{min} is set to be 1 for the number of layers and $2 \times 10^{-4}s$ for the time step.

The optimization path generated by the algorithm follows the rule of slower printing speed and larger number of layers and eventually stops at the boundary governed by the constraints as shown in Figure 4. The optimization result translates to printing more slowly and slicing the wall more finely in order to reduce the shape error, both of which are intuitively plausible. Of course, on practical grounds, the trade-off is that the overall printing of the part takes longer.

Note that in this example the purely geometric error, defined as the shape error under no deformation, is equal to zero due to the (nominally) rectangular shape of the printed part. Therefore, the thermomechanical response during the building process is responsible for the entirety of the shape error. Algorithm 2 successfully converges to the global minimum

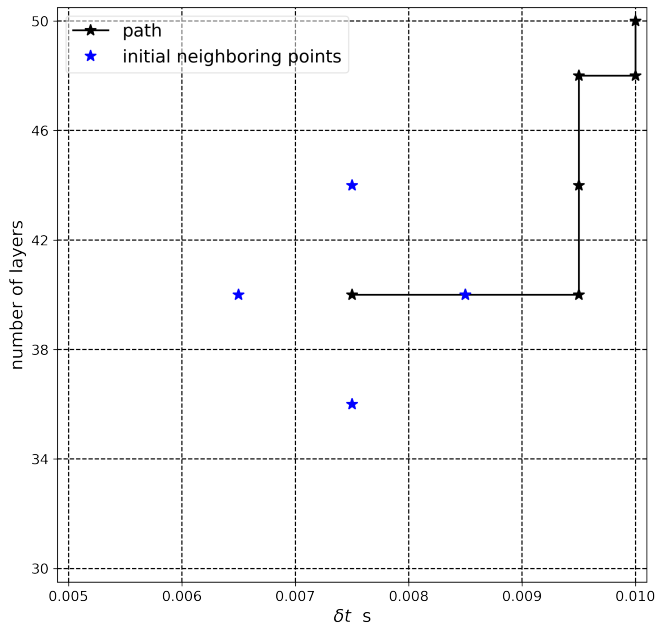


Figure 4: Two-dimensional wall optimization path in the optimization space with method of local variations

for the objective function within the bounds in (29). The left plot in Figure 7 is the filled contour plot of the objective function with respect to the two process parameters, constructed through exhaustive sampling. Evident in the figure is the smoothness of the objective function which leads to successful convergence of the optimization procedure. Further, the objective function is monotonic in both process parameters within the bounds, making it easy to find neighboring points with a smaller objective function value.

The initial sampling is important in the convergence of the Bayesian optimization. Here, four corner points are selected in the bounded optimization space. The mean value and expected improvement acquisition function value contour for each iteration are shown in Figure 5 and 6. The ground truth objective and the prediction by the surrogate model at termination are displayed in Figure 7, where the black dots in the surrogate contour are the sampled points. Notice that the objective value plotted is the scaled value of the $-f_h$ since Algorithm 3 solves a equivalent maximization problem, as explained in Section 5.2. Thus, the maximum value shown indeed corresponds to the minimal shape error. In this case, the four initial points suffice in generating a decent surrogate model and the algorithm terminates in 2 iterations as the predicted optimal variables produced by two consecutive iterations are close enough, at the top-right corner in Figure 7. The optimal design variables are found to be 50 layers and 0.01s, which translates to layer thickness of 0.2mm and a

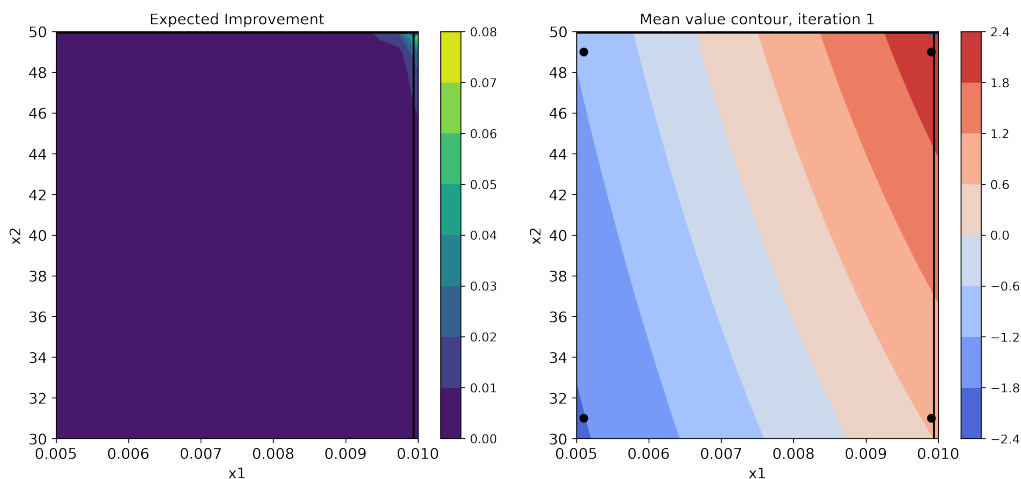


Figure 5: Two-dimensional wall Bayesian optimization, expected improvement and mean value contour, iteration 1. The axes x_1 and x_2 are the number of layers ($10/\Delta y$) and temporal step size δt , respectively, as in (29).

printing speed of $0.057m/s$.

6.2 Two-dimensional wall with hole after heat dissipation

This example concerns the simulation of printing a two-dimensional wall with a circular hole. The width of the wall is $15mm$ and the height is $10mm$. A quarter-circular hole of radius $r = 3mm$ is situated at the top-right corner of the wall, as in Figure 8. Due to the curved shape, hanging nodes are used in the vicinity of the circular boundary mesh.

The shape error is measured along the circular edge. Specifically, Γ_S^t in (17) is the *step-edge* approximation of the quarter-circular hole in the reference configuration, which is defined as the edges formed by connecting the mid-points of the actual printed-edge approximation of the hole, as in Figure 9. This definition ensures that in the reference configuration the length of Γ_S^t , under mesh refinement, becomes closer to the arc length of the circle $\pi r/2$, in contrast to the length of the actual mesh boundary, which is always equal to $2r$. The local shape error $d(\mathbf{X}, \mathbf{u}) - \bar{d}(\mathbf{X})$ in (18) is defined as the deviation in radius of the step-edge approximation from the circle of the designed shape. The critical length L_c here is chosen to be the radius r of the same circle.

Algorithm 1 is first applied to determine the optimal convection coefficient $h \in [30, 55]W/m^2K$, where $\alpha_0 = 1$, $\rho = 0.5$ and $\eta = 0.1$. The time-step size for printing a full element is set to $0.006s$, equivalent to a printing speed of $62.5mm/s$, while the number of layers is fixed

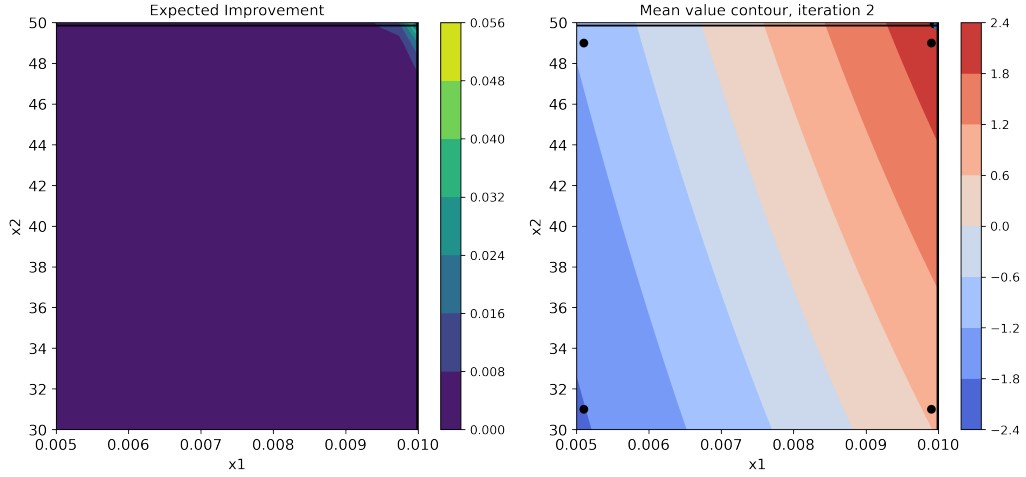


Figure 6: Two-dimensional wall Bayesian optimization, expected improvement and mean value contour, iteration 2. The black dots represent sampled points.

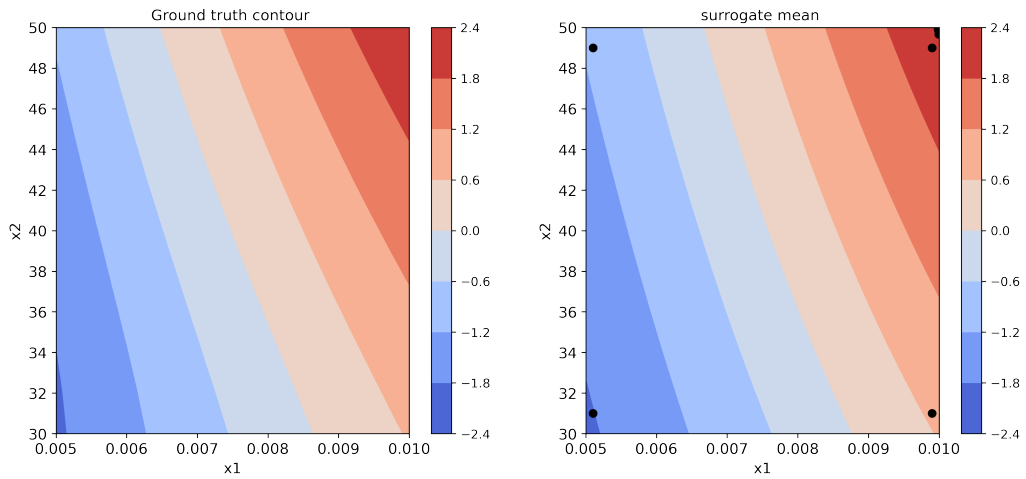


Figure 7: Two-dimensional wall Bayesian optimization, ground truth and surrogate objective.

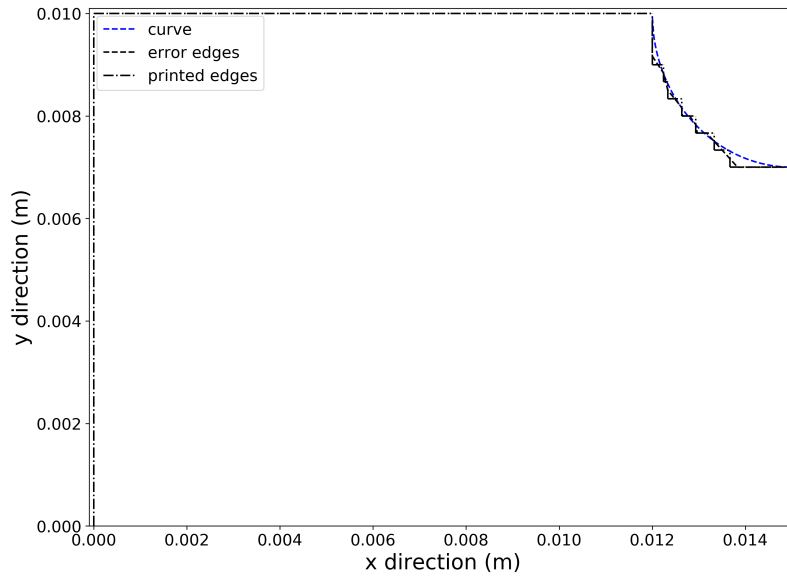


Figure 8: Boundary and error edges for two-dimensional wall with hole

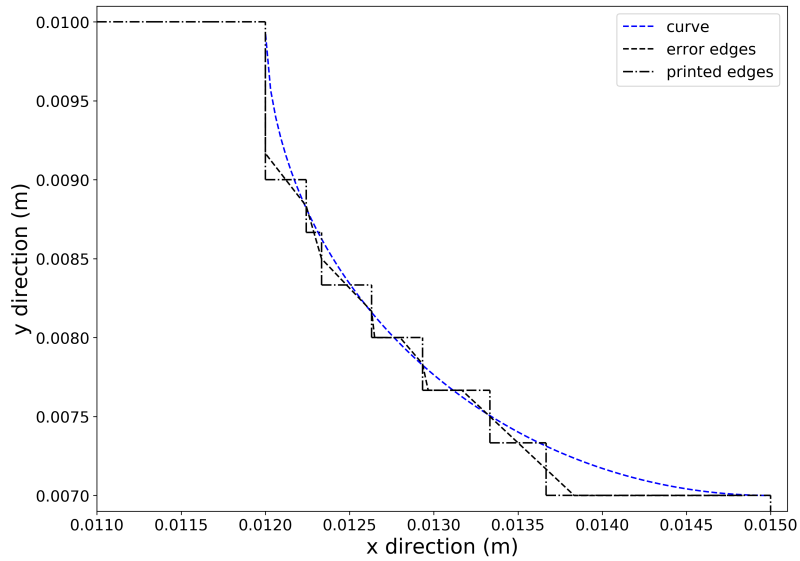


Figure 9: Error edges for two-dimensional wall with hole zoomed in

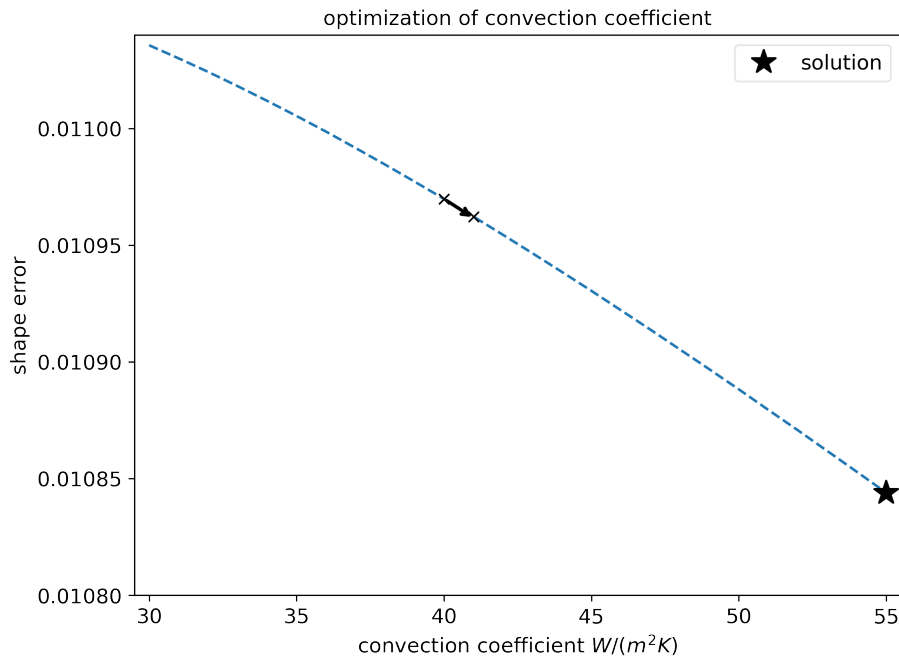


Figure 10: Two-dimensional wall with hole: Optimization of convection coefficient

at 30. Again, the sensitivity $\frac{df_h}{dy}$ is computed based on the method described in Section 4 and the appendix. However, additional care needs to be taken due to the presence of hanging nodes around the quarter-circle. As described towards the end of Section 2.2, a ratio is maintained for the displacement and temperature of a hanging node that resides on an edge with two other nodes at the end of the edge. Naturally, the sensitivity of the displacement and temperature of the hanging node is required to maintain the same ratio. The initial convection coefficient h_0 is set to $40W/m^2K$. The optimization path is shown in Figure 10.

The two gradient-free optimization algorithms are applied to the optimization of the printing speed and layer thickness for $h = 40W/m^2K$. The bounds of the process parameters are set to

$$\begin{aligned} 0.20mm &\leq \Delta y \leq 0.33mm , \\ 0.004s &\leq \delta t \leq 0.009s . \end{aligned} \tag{30}$$

The remaining algorithmic parameter setup is as in the previous example. However, the presence of the circular hole causes the shape error to have a more complex relation to the number of layers. Indeed, it is evident that the shape error here is nonzero in the reference configuration with no deformation. This is because the shape error is measured against the ideal quarter-circle on rectangular boundary elements. The referential shape error is

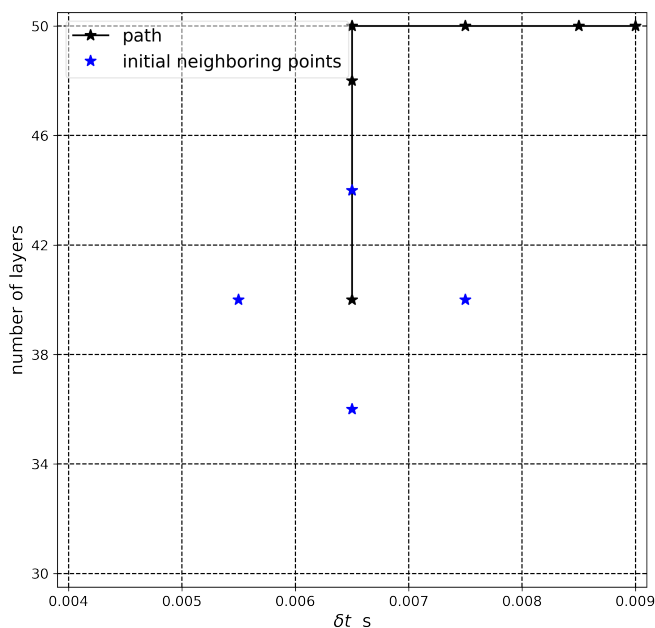


Figure 11: Two-dimensional wall with hole: Optimization path with method of local variations

intrinsic to the layered approximation of a circular curve. The shape error is also affected by the slicing algorithm that determines where each layer should stop at the boundary of the circle. The discrete nature of the number of layers, slicing algorithm and rectangular approximation of a circle lead to a non-monotonic relationship between the shape error and the number of layers. We refer to the shape error in reference configuration with no deformation as the geometric error. The geometric error does not change the general trend of how the process parameters affect the shape error, as we show later in the section, because the thermomechanical shape error caused by the AM building process itself is significantly larger. More discussion on this topic can be found in [26, 86, 87].

The optimization path generated by the method of local variations is shown in Figure 11, where the initial step size is $0.001s$ for the print velocity and 4 for the number of layers. Starting from the point $(0.0065s, 40)$ in printing speed/number of layer-space, the optimization method traces a path to $(0.0065s, 50)$ followed by consecutively smaller speed until the boundary is hit at $(0.009s, 50)$. The step size τ_k keeps decreasing to τ_{min} (1 for the number of layers) as no neighboring point produces smaller objective function values and eventually the iteration stops. Therefore, the optimal variables given by the method of local variations are $(0.009s, 50)$, which are optimal as shown in the filled contour plot on the left in Figure 14.

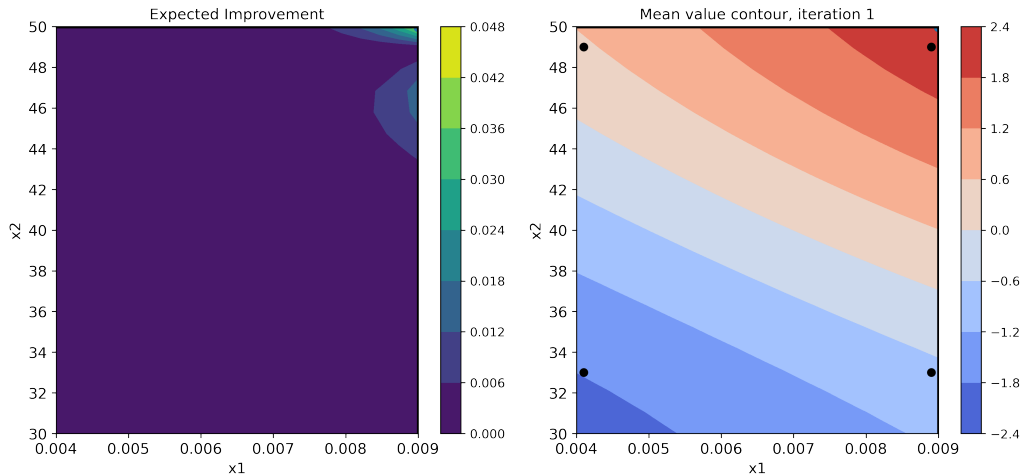


Figure 12: Two-dimensional wall with hole: Bayesian optimization, expected improvement and mean value contour, iteration 1. The black dots are the sampled points.

Next, the Bayesian optimization algorithm is applied to the same problem, starting from four initial sample points. The mean value and expected improvement contour for selected iterations are shown in Figures 12 and 13, respectively. The ground truth objective and the prediction by the surrogate model at the time of termination are displayed in Figure 14, where the black dots in the surrogate contour are the sampled points. It is emphasized again that the objective shown in the plots are the scaled values of negative shape error.

While Algorithm 3 still converges in two iterations, it is clear that the predicted mean value contour is not an accurate depiction of the ground truth, as shown in Figure 14. However, since the algorithm only strives to find the optimal design variables, it terminates as the point $(0.009s, 50)$ at the top right corner is found repeatedly. If we have nine initial sample points, as shown in Figure 15, an overall more accurate surrogate model for f_h of Δy and δt can be found.

The results from both examples predict a better finish quality with higher cooling rate (convection coefficient) within a realistic range. They both point to reduced shape error with slower printing and more layers. These seemingly obvious results would be considerably more complicated given real application constraints such as production time and cost associated with increased number of layers. In addition, the wall with a circular hole example illustrates that both the process parameters studied in this work and the pure geometric design of the object contribute to the shape error. The gradient-based optimization, while costly, is more accurate and can scale well. It can also rely on the

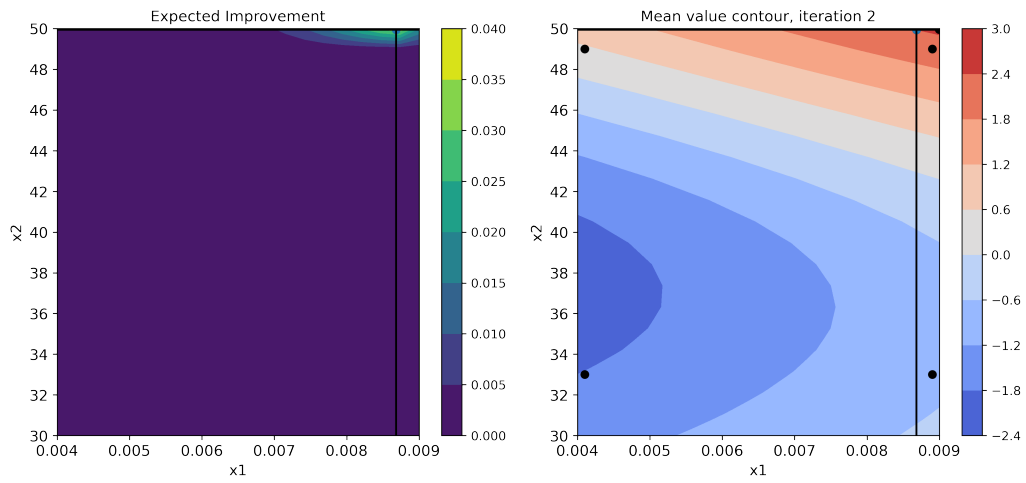


Figure 13: Two-dimensional wall with hole Bayesian optimization, expected improvement and mean value contour, iteration 2. The intersection of horizontal and vertical lines are the new sampled points to be included in the surrogate model.

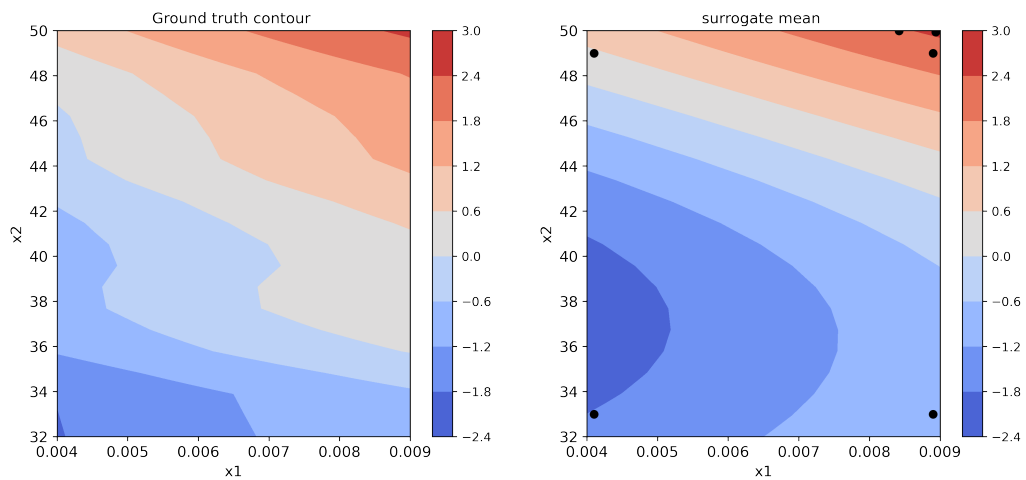


Figure 14: Two-dimensional wall with hole: Bayesian optimization: Ground truth and surrogate objective

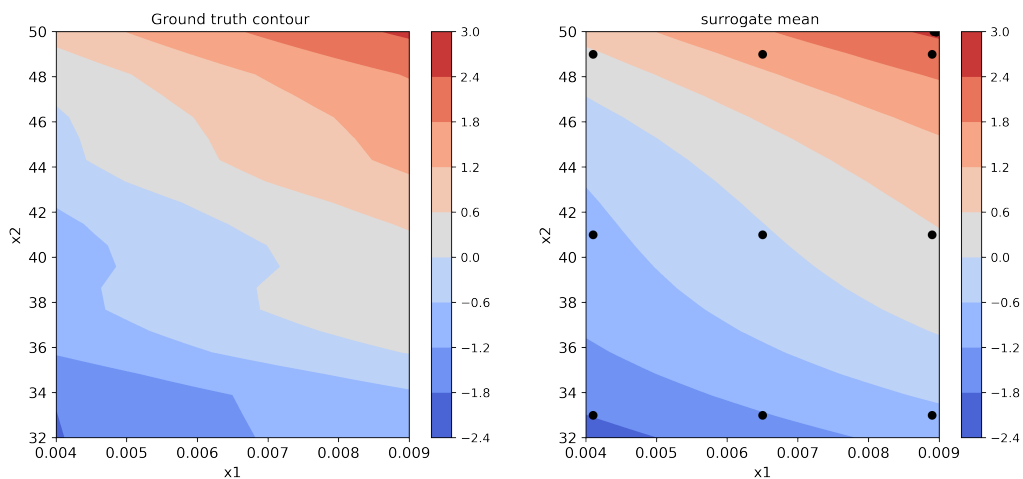


Figure 15: Two-dimensional wall with hole: Bayesian optimization, 9 initial samples, ground truth and surrogate objective

wealth of optimization theories to guarantee local minimum convergence [83]. However, computing the sensitivities takes effort and is in general less flexible to new variables and problems.

Gradient-free optimization is a promising alternative, particularly Bayesian optimization. This approach eliminates the need to compute complicated sensitivities, and thus can be easily adapted to different simulation models, including ones different from ours. Accompanied by physical experiments for validation, it can be useful in practice. In this work, we rely on a fully coupled thermomechanical finite element model to generate sample points. In practice, lower fidelity weakly coupled models can work well and further reduce the cost of each simulation. Bayesian optimization can be applied directly to those more commonly used production models. We point out that if the optimization space is large, the method using GP might not scale well.

7 Conclusions

In this paper, design optimization methods for AM process parameters have been proposed based on finite element simulation. To address the diverse set of variables, both gradient-based and gradient-free optimization methods have been proposed and implemented. While the objective is chosen to be shape error, the framework can be adapted to other design goals. The gradient-based approach relies on fully discretized reduced space formulation of the balance equations to obtain sensitivities. For gradient-free optimization, a local search algorithm and a Bayesian optimization algorithm using Gaussian process surrogate

models and expected improvement acquisition functions are presented. Numerical experiments demonstrate that these optimization methods can yield physically plausible results efficiently. Line search gradient descent algorithm is applied to convection coefficient and gradient-free algorithms are deployed for layer thickness and printing speed. These flexible methods can be easily extended to other design variables. And in the case of gradient-free optimization, other finite element models, particularly mature uncoupled three-dimensional ones, can be easily adopted. Surrogate models using NN can also be developed.

References

- [1] O.A. Mohamed, S.H. Masood, and J.L. Bhowmik. Optimization of fused deposition modeling process parameters: A review of current research and future prospects. *Advances in Manufacturing*, 3:42–53, March 2015.
- [2] I. Gibson, D.W. Rosen, and B. Stucker. *Additive Manufacturing Technologies*. Springer, New York, 2014.
- [3] C.K. Chua, K.F. Leong, and C.S. Lim. *Rapid prototyping: principles and applications (with companion CD-ROM)*. World Scientific Publishing Company, Singapore, 2010.
- [4] S. Upcraft and R. Fletcher. The rapid prototyping technologies. *Assembly Automation*, 23:318–330, December 2003.
- [5] S. Mansour and R. Hague. Impact of rapid manufacturing on design for manufacture for injection moulding. *Proceedings of the Institution of Mechanical Engineers, Part B: Journal of Engineering Manufacture*, 217:453–461, April 2003.
- [6] N. Hopkinson, R.J. Hague, and P.M. Dickens. *Rapid manufacturing: An Industrial Revolution for the Digital Age*. John Wiley and Sons, 2006.
- [7] B. Thavornyutikarn, N. Chantarapanich, K. Sitthiseripratip, G.A. Thouas, and Q. Chen. Bone tissue engineering scaffolding: Computer-aided scaffolding techniques. *Progress in Biomaterials*, 3:61–102, December 2014.
- [8] S.H. Ahn, M. Montero, D. Odell, S. Roundy, and P.K. Wright. Anisotropic material properties of fused deposition modeling ABS. *Rapid Prototyping Journal*, 8:248–257, October 2002.
- [9] M.M. Francois, A. Sun, W.E. King, N.J. Henson, D. Tourret, C.A. Bronkhorst, N.N Carlson, C.K. Newman, T.S. Haut, J. Bakosi J, and J.W. Gibbs. Modeling of additive manufacturing processes for metals: Challenges and opportunities. *Current Opinion in Solid State and Materials Science*, 21:SAND–2017–6832J, January 2017.
- [10] W. King, A.T. Anderson, R.M. Ferencz, N.E. Hodge, C. Kamath, and S.A. Khairallah. Overview of modelling and simulation of metal powder bed fusion process at Lawrence Livermore National Laboratory. *Materials Science and Technology*, 31:957–968, June 2015.

- [11] B. Schoinochoritis, D. Chantzis, and K. Salonitis. Simulation of metallic powder bed additive manufacturing processes with the finite element method: A critical review. *Proceedings of the Institution of Mechanical Engineers, Part B: Journal of Engineering Manufacture*, 231:96–117, January 2017.
- [12] F. Hajjalizadeh and A. Ince. Short review on modeling approaches for metal additive manufacturing process. *Material Design and Processing Communications*, 2:e56, March 2019.
- [13] S.J. Kalita, S. Bose, H.L. Hosick, and A. Bandyopadhyay. Development of controlled porosity polymer-ceramic composite scaffolds via fused deposition modeling. *Materials Science and Engineering: C*, 23:611–620, October 2003.
- [14] B. Schoinochoritis, D. Chantzis, and K. Salonitis. Simulation of metallic powder bed additive manufacturing processes with the finite element method: A critical review. *Proceedings of the Institution of Mechanical Engineers, Part B: Journal of Engineering Manufacture*, 231:96–117, January 2017.
- [15] S. Jayanath and A. Achuthan. A computationally efficient finite element framework to simulate additive manufacturing processes. *Journal of Manufacturing Science and Engineering*, 140, April 2018.
- [16] P. Michaleris. Modeling metal deposition in heat transfer analyses of additive manufacturing processes. *Finite Elements in Analysis and Design*, 86:51–60, September 2014.
- [17] Y. Zhang and Y.K. Chou. Three-dimensional finite element analysis simulations of the fused deposition modelling process. *Proceedings of the Institution of Mechanical Engineers, Part B: Journal of Engineering Manufacture*, 220:1663–1671, October 2006.
- [18] N. Patil, D. Pal, and B. Stucker. A new finite element solver using numerical eigen modes for fast simulation of additive manufacturing processes. In *2013 International Solid Freeform Fabrication Symposium*. University of Texas at Austin, August 2013.
- [19] J. Ding, P. Colegrove, J. Mehnen, S. Williams, F. Wang, and P.S. Almeida. A computationally efficient finite element model of wire and arc additive manufacture. *The International Journal of Advanced Manufacturing Technology*, 70:227–236, January 2014.
- [20] F. Monteverchi, G. Venturini, A. Scippa, and G. Campatelli. Finite element modelling of wire-arc-additive-manufacturing process. *Procedia Cirp*, 55:109–114, January 2016.
- [21] E.R. Denlinger, J. Irwin, and P. Michaleris. Thermomechanical modeling of additive manufacturing large parts. *Journal of Manufacturing Science and Engineering*, 136, December 2014.
- [22] E.R. Denlinger, M. Gouge, J. Irwin, and P. Michaleris. Thermomechanical model development and in situ experimental validation of the laser powder-bed fusion process. *Additive Manufacturing*, 16:73–80, August 2017.

- [23] I.A. Roberts, C.J. Wang, R. Esterlein, M. Stanford, and D.J. Mynors. A three-dimensional finite element analysis of the temperature field during laser melting of metal powders in additive layer manufacturing. *International Journal of Machine Tools and Manufacture*, 49:916–923, October 2009.
- [24] Q. Yang, P. Zhang, L. Cheng, Z. Min, M. Chyu, and A.C. To. Finite element modeling and validation of thermomechanical behavior of Ti-6Al-4V in directed energy deposition additive manufacturing. *Additive Manufacturing*, 12:169–177, October 2016.
- [25] S. Kolossov, E. Boillat, R. Glardon, P. Fischer, and M. Locher. 3D FE simulation for temperature evolution in the selective laser sintering process. *International Journal of Machine Tools and Manufacture*, 44:117–123, February 2004.
- [26] J. Wang and P. Papadopoulos. Coupled thermomechanical analysis of fused deposition using the finite element method. *Finite Elements in Analysis and Design*, 197:103607, December 2021.
- [27] S.H. Masood. Intelligent rapid prototyping with fused deposition modelling. *Rapid Prototyping Journal*, 2:24–33, March 1996.
- [28] J.R. Groza and J.F. Shackelford. *Materials Processing Handbook*. CRC press, Boca Raton, 2007.
- [29] C. Bellehumeur, L. Li, Q. Sun, and P. Gu. Modeling of bond formation between polymer filaments in the fused deposition modeling process. *Journal of Manufacturing Processes*, 6:170–178, January 2004.
- [30] J.M. Chacón, M.A. Caminero, E. García-Plaza, and P.J. Núñez. Additive manufacturing of PLA structures using fused deposition modelling: Effect of process parameters on mechanical properties and their optimal selection. *Materials and Design*, 124:143–157, June 2017.
- [31] T. Nancharaiah, D.R. Raju, and V.R. Raju. An experimental investigation on surface quality and dimensional accuracy of FDM components. *International Journal on Emerging Technologies*, 1:106–111, January 2010.
- [32] D. Horvath, R. Noorani, and M. Mendelson. Improvement of surface roughness on abs 400 polymer using design of experiments (DOE). *Materials Science Forum*, 561:2389–2392, 2007.
- [33] C.C. Wang, T.W. Lin, and S.S. Hu. Optimizing the rapid prototyping process by integrating the Taguchi method with the gray relational analysis. *Rapid Prototyping Journal*, 13(5):304–315, October 2007.
- [34] K.P. Thrimurthulu, P.M. Pandey, and N.V. Reddy. Optimum part deposition orientation in fused deposition modeling. *International Journal of Machine Tools and Manufacture*, 44:585–594, May 2004.

- [35] T. Mukherjee, W. Zhang, and T. DebRoy. An improved prediction of residual stresses and distortion in additive manufacturing. *Computational Materials Science*, 126:360–372, October 2017.
- [36] A. Foroozmehr, M. Badrossamay, E. Foroozmehr, and S.I. Golabi. Finite element simulation of selective laser melting process considering optical penetration depth of laser in powder bed. *Materials and Design*, 89:255–263, January 2016.
- [37] A.P. West, S.P. Sambu, and D.W. Rosen. A process planning method for improving build performance in stereolithography. *Computer-Aided Design*, 33:65–79, January 2001.
- [38] G. Strano, L. Hao, R.M. Everson, and K.E. Evans. Surface roughness analysis, modelling and prediction in selective laser melting. *Journal of Materials Processing Technology*, 213:589–597, April 2013.
- [39] G. Onwubolu and F. Rayegani. Characterization and optimization of mechanical properties of ABS parts manufactured by the fused deposition modelling process. *International Journal of Manufacturing Engineering*, pages 1–13, November 2014.
- [40] M. Domingo-Espin, J.M. Puigoriol-Forcada, A.A. Garcia-Granada, J. Llumà, S. Borros, and G. Reyes. Mechanical property characterization and simulation of fused deposition modeling polycarbonate parts. *Materials and Design*, 83:670–677, October 2015.
- [41] K.C. Ang, K.F. Leong, C.K. Chua, and M. Chandrasekaran. Investigation of the mechanical properties and porosity relationships in fused deposition modelling-fabricated porous structures. *Rapid Prototyping Journal*, 12:100–105, March 2006.
- [42] A.K. Sood, R.K. Ohdar, and S.S. Mahapatra. Parametric appraisal of mechanical property of fused deposition modelling processed parts. *Materials and Design*, 31:287–295, January 2010.
- [43] G. Percoco, F. Lavecchia, and L.M. Galantucci. Compressive properties of fdm rapid prototypes treated with a low cost chemical finishing. *Research Journal of Applied Sciences, Engineering and Technology*, 4:3838–3842, October 2012.
- [44] F. Rayegani and G.C Onwubolu. Fused deposition modelling (FDM) process parameter prediction and optimization using group method for data handling (GMDH) and differential evolution (DE). *The International Journal of Advanced Manufacturing Technology*, 73:509–519, July 2014.
- [45] S.H. Masood, K. Mau, and W.Q. Song. Tensile properties of processed FDM polycarbonate material. *Materials Science Forum*, 654-656:2556–2559, June 2010.
- [46] A. Arivazhagan, S. Masood, and I. Sbarski. Dynamic mechanical analysis of fused deposition modelling processed polycarbonate. *Annual Technical Conference - ANTEC, Conference Proceedings*, 1:950–955, January 2011.

- [47] A. Arivazhagan and S.H. Masood. Dynamic mechanical properties of ABS material processed by fused deposition modelling. *International Journal of Engineering Research and Applications*, 2:2009–2014, May 2012.
- [48] R. Anitha, S. Arunachalam, and P. Radhakrishnan. Critical parameters influencing the quality of prototypes in fused deposition modelling. *Journal of Materials Processing Technology*, 118:385–388, December 2001.
- [49] A.K. Sood, R.K. Ohdar, and S.S. Mahapatra. Improving dimensional accuracy of fused deposition modelling processed part using grey Taguchi method. *Materials and Design*, 30:4243–4252, December 2009.
- [50] B.H. Lee, J. Abdullah, and Z.A. Khan. Optimization of rapid prototyping parameters for production of flexible abs object. *Journal of Materials Processing Technology*, 169:54–61, October 2005.
- [51] A.K. Sood, R.K. Ohdar, and S.S. Mahapatra. Experimental investigation and empirical modelling of FDM process for compressive strength improvement. *Journal of Advanced Research*, 3:81–90, January 2012.
- [52] H.S Cho, W.S. Park, B.W. Choi, and M.C. Leu. Determining optimal parameters for stereolithography processes via genetic algorithm. *Journal of Manufacturing Systems*, 19:18, 2000.
- [53] D. Syrlybayev, B. Zharylkassyn, A. Seisekulova, A. Perveen, and D. Talamona. Optimization of the warpage of fused deposition modeling parts using finite element method. *Polymers*, 13(21):3849, January 2021.
- [54] J. Gockel, J. Beuth, and K. Taminger. Integrated control of solidification microstructure and melt pool dimensions in electron beam wire feed additive manufacturing of Ti-6Al-4V. *Additive Manufacturing*, 1:119–126, October 2014.
- [55] T.A. Krol, M.F. Zaeh, and C. Seidel. Optimization of supports in metal-based additive manufacturing by means of finite element models. *23rd Annual International Solid Freeform Fabrication Symposium - An Additive Manufacturing Conference, SFF 2012*, pages 707–718, 01 2012.
- [56] A. Vasinonta, J.L. Beuth, and M.L. Griffith. A process map for consistent build conditions in the solid freeform fabrication of thin-walled structures. *Journal of Manufacturing Science and Engineering*, 123:615–622, August 2000.
- [57] J. Yin, W. Liu, Y. Cao, L. Zhang, J. Wang, Z. Li, Z. Zhao, and P. Bai. Rapid prediction of the relationship between processing parameters and molten pool during selective laser melting of cobalt-chromium alloy powder: Simulation and experiment. *Journal of Alloys and Compounds*, 892:162200, February 2022.

- [58] G. Vastola, G. Zhang, Q.X. Pei, and Y.W. Zhang. Controlling of residual stress in additive manufacturing of Ti-6Al-4V by finite element modeling. *Additive Manufacturing*, 12:231–239, October 2016.
- [59] A.H. Nickel, D.M. Barnett, and F.B. Prinz. Thermal stresses and deposition patterns in layered manufacturing. *Materials Science and Engineering: A*, 317:59–64, October 2001.
- [60] A. Alafaghani, A. Qattawi, B. Alrawia, and A. Guzman. Experimental optimization of fused deposition modelling processing parameters: A design-for-manufacturing approach. *Procedia Manufacturing*, 10:791–803, December 2017.
- [61] Y. Zhang and Y.K. Chou. 3D FEA simulations of fused deposition modeling process. In *ASME 2006 International Manufacturing Science and Engineering Conference*, pages 1121–1128, January 2006.
- [62] H. D. Morgan, J. A. Cherry, S. Jonnalagadda, D. Ewing, and J. Sieng. Part orientation optimisation for the additive layer manufacture of metal components. *The International Journal of Advanced Manufacturing Technology*, 86:1679–1687, September 2016.
- [63] J. Wang and N. Zabaras. A Bayesian inference approach to the inverse heat conduction problem. *International Journal of Heat and Mass Transfer*, 47:3927–3941, August 2004.
- [64] A. Mathern, O. S. Steinholtz, A. Sjöberg, et al. Multi-objective constrained bayesian optimization for structural design. *Structural and Multidisciplinary Optimization*, 63:689–701, February 2021.
- [65] R. Calandra, A. Seyfarth, J. Peters, and M. P. Deisenroth. Bayesian optimization for learning gaits under uncertainty. *Annals of Mathematics and Artificial Intelligence*, 76:5–23, February 2016.
- [66] J. Bernardo, M. J. Bayarri, J. O. Berger, A. P. Dawid, D. Heckerman, A. F. Smith, and M. West. Optimization under unknown constraints. *Bayesian Statistics*, 9:229, October 2011.
- [67] M. Zuluaga, G. Sergeant, A. Krause, and M. Püschel. Active learning for multi-objective optimization. In *International Conference on Machine Learning*, pages 462–470. PMLR, February 2013.
- [68] M. Zhang, A. Parnell, D. Brabazon, and A. Benavoli. Bayesian optimisation for sequential experimental design with applications in additive manufacturing. *arXiv preprint arXiv:2107.12809*, July 2021.
- [69] S. Goguelin, V. Dhokia, and J. M. Flynn. Bayesian optimisation of part orientation in additive manufacturing. *International Journal of Computer Integrated Manufacturing*, 34:1263–84, December 2021.

- [70] *Design of Mechanical Metamaterials via Constrained Bayesian Optimization*, volume Volume 2A: 44th Design Automation Conference of *International Design Engineering Technical Conferences and Computers and Information in Engineering Conference*, 08 2018. V02AT03A029.
- [71] T. Xue, T.J. Wallin, Y. Menguc, S. Adriaenssens, and M. Chiaramonte. Machine learning generative models for automatic design of multi-material 3D printed composite solids. *Extreme Mechanics Letters*, 41:100992, November 2020.
- [72] N. Hertlein, K. Vemaganti, and S. Anand. Bayesian optimization of energy-absorbing lattice structures for additive manufacturing. In *ASME International Mechanical Engineering Congress and Exposition*, volume 84539, 2020.
- [73] S. Mondal, D. Gwynn, A. Ray, and A. Basak. Investigation of melt pool geometry control in additive manufacturing using hybrid modeling. *Metals*, 10:683, May 2020.
- [74] Y. Xiong, P. L. Duong, D. Wang, S. I. Park, Q. Ge, N. Raghavan, and D. W. Rosen. Data-driven design space exploration and exploitation for design for additive manufacturing. *Journal of Mechanical Design*, 141, October 2019.
- [75] I. Baturynska, O. Semeniuta, and K. Martinsen. Optimization of process parameters for powder bed fusion additive manufacturing by combination of machine learning and finite element method: A conceptual framework. In *Procedia Cirp*, volume 67, pages 227–32, January 2018.
- [76] S. Reese and S. Govindjee. Theoretical and numerical aspects in the thermo-viscoelastic material behaviour of rubber-like polymers. *Mechanics of Time-Dependent Materials*, 1:357–396, December 1997.
- [77] P.M. Pandey, N.V. Reddy, and S.G. Dhande. Improvement of surface finish by staircase machining in fused deposition modeling. *Journal of Materials Processing Technology*, 132:323–331, January 2003.
- [78] Peter I Frazier. A tutorial on bayesian optimization. *arXiv preprint arXiv:1807.02811*, 2018.
- [79] E. Polak. *Computational Methods in Optimization: A Unified Approach*. Academic press, New York, 1971.
- [80] P. I. Frazier. Bayesian optimization. In *Recent advances in optimization and modeling of contemporary problems*, pages 255–278. Informs, October 2018.
- [81] Bobak Shahriari, Kevin Swersky, Ziyu Wang, Ryan P Adams, and Nando De Freitas. Taking the human out of the loop: A review of bayesian optimization. *Proceedings of the IEEE*, 104(1):148–175, 2015.
- [82] E. Brochu, V. M. Cora, and N. De Freitas. A tutorial on bayesian optimization of expensive cost functions, with application to active user modeling and hierarchical reinforcement learning. *arXiv preprint arXiv:1012.2599*, December 2010.

- [83] J. Nocedal and S. Wright. *Numerical Optimization*. Springer-Verlag, New York, 2006.
- [84] F. Pedregosa, G. Varoquaux, A. Gramfort, V. Michel, B. Thirion, O. Grisel, M. Blondel, P. Prettenhofer, R. Weiss, V. Dubourg, J. Vanderplas, A. Passos, D. Cournapeau, M. Brucher, M. Perrot, and E. Duchesnay. Scikit-learn: Machine learning in Python. *Journal of Machine Learning Research*, 12:2825–2830, 2011.
- [85] L. Buitinck, G. Louppe, M. Blondel, F. Pedregosa, A. Mueller, O. Grisel, V. Niculae, P. Prettenhofer, A. Gramfort, J. Grobler, R. Layton, J. VanderPlas, A. Joly, B. Holt, and G. Varoquaux. API design for machine learning software: experiences from the scikit-learn project. In *ECML PKDD Workshop: Languages for Data Mining and Machine Learning*, pages 108–122, 2013.
- [86] Young-Hyu Choi, Cheol-Min Kim, Hwan-Seock Jeong, and Jeong-Ho Youn. Influence of bed temperature on heat shrinkage shape error in fdm additive manufacturing of the abs-engineering plastic. *World Journal of Engineering and Technology*, 4(3):186–192, 2016.
- [87] Ratnadeep Paul, Sam Anand, and Frank Gerner. Effect of Thermal Deformation on Part Errors in Metal Powder Based Additive Manufacturing Processes. *Journal of Manufacturing Science and Engineering*, 136(3):031009, 03 2014.

Appendix: Finite element matrices

The spatial approximation of the dependent variables and their derivatives employs standard piecewise polynomials stemming from 4-node isoparametric element interpolation in two dimensions.

The values of the material parameters are listed in Table 1. The material reference temperature is denoted by $\theta_{0,m}$. The parameters were estimated through least squares fitting of the experimental data for the temperature range of the simulations in this work.

Material parameter	Numerical values	Units
a	−5.5	—
b	1.0	—
$\theta_{0,m}$	475	K
$E_{0,m}$	250	MPa

Table 1: *Material parameters for the simplified constitutive function in Equation (6)*

The element-level matrices in (14) are

$$\begin{aligned}
 [\mathbf{M}_u^e] &= \int_{\Omega_0^e} [\mathbf{N}_u^e]^T \rho_0 [\mathbf{N}_u^e] dV , \\
 [\mathbf{R}_{u,n+1}^e] &= \int_{\Omega_0^e} [\mathbf{B}_u^e]^T \langle \boldsymbol{\sigma}_{n+1}^e \rangle dV , \\
 [\mathbf{F}_{n+1}^e] &= \int_{\Omega_0^e} [\mathbf{N}_u^e]^T \rho_0 [\mathbf{b}_{n+1}] dV + \int_{\Gamma_{N,0}^u \cap \partial\Omega_0^e} [\mathbf{N}_u^e]^T [\bar{\mathbf{p}}_{n+1}^e] dA , \\
 [\mathbf{T}_{n+1}^e] &= \int_{\Omega_0^e} [\mathbf{N}_t^e]^T c_{n+1}^e [\mathbf{N}_t^e] dV , \\
 [\mathbf{M}_t^e] &= \int_{\Omega_0^e} k [\mathbf{B}_t^e]^T [\mathbf{B}_t^e] dV - \int_{\Gamma_{N,0}^t \cap \partial\Omega_0^e} [\mathbf{N}_t^e]^T h [\mathbf{N}_t^e] dA , \\
 [\mathbf{R}_{t,n+1}^e] &= - \int_{\Omega_0^e} [\mathbf{N}_t^e]^T \theta_{n+1}^e \langle \mathbf{M}_{n+1}^e \rangle^T \langle \dot{\boldsymbol{\epsilon}}_{n+1}^e \rangle dV , \\
 [\mathbf{Q}_{n+1}^e] &= \int_{\Omega_0^e} [\mathbf{N}_t^e]^T \rho_0 r_{n+1} dV - \int_{\Gamma_{N,0}^t \cap \partial\Omega_0^e} [\mathbf{N}_t^e]^T h \theta_\infty dA ,
 \end{aligned} \tag{A.1}$$

and also

$$[\mathbf{K}_{u,n+1}^{e,(k)}] = \frac{4}{\Delta t_n^2} \int_{\Omega_0^e} [\mathbf{N}_u^e]^T \rho_0 [\mathbf{N}_u^e] dV + \int_{\Omega_0^e} [\mathbf{B}_u^e]^T \left[\left(\frac{\partial \boldsymbol{\sigma}}{\partial \boldsymbol{\epsilon}} \right)_{n+1}^{e,(k)} \right] [\mathbf{B}_u^e] dV , \tag{A.2}$$

$$[\mathbf{K}_{t,n+1}^{e,(k)}] = \int_{\Omega_0^e} [\mathbf{B}_u^e]^T \left\langle \left(\frac{\partial \boldsymbol{\sigma}}{\partial \theta} \right)_{n+1}^{e,(k)} \right\rangle [\mathbf{N}_t^e] dV , \tag{A.3}$$

$$[\mathbf{A}_{u,n+1}^{e,(k)}] = \int_{\Omega_0^e} [\mathbf{N}_t^e]^T \left\langle \left(\frac{\partial c}{\partial \boldsymbol{\epsilon}} \right)_{n+1}^{e,(k)} \right\rangle \dot{\theta}_{n+1}^{e,(k)} [\mathbf{B}_u^e] dV \quad (\text{A.4})$$

$$- \frac{2}{\Delta t_n} \int_{\Omega_0^e} [\mathbf{N}_t^e]^T \theta_{n+1}^{e,(k)} \langle \mathbf{M}_{n+1}^{e,(k)} \rangle^T [\mathbf{B}_u^e] dV \quad (\text{A.5})$$

$$- \int_{\Omega_0^e} [\mathbf{N}_t^e]^T \theta_{n+1}^{e,(k)} \langle \dot{\boldsymbol{\epsilon}}_{n+1}^{e,(k)} \rangle^T \left[\left(\frac{\partial \mathbf{M}}{\partial \boldsymbol{\epsilon}} \right)_{n+1}^{e,(k)} \right] [\mathbf{B}_u^e] dV, \quad (\text{A.6})$$

$$[\mathbf{A}_{t,n+1}^{e,(k)}] = \int_{\Omega_0^e} [\mathbf{N}_t^e]^T \left[\left(\frac{\partial c}{\partial \theta} \right)_{n+1}^{e,(k)} \right] \dot{\theta}_{n+1}^{e,(k)} [\mathbf{N}_t^e] dV \quad (\text{A.7})$$

$$+ \int_{\Omega_0^e} [\mathbf{N}_t^e]^T \frac{c_{n+1}^{e,(k)}}{\Delta t_n} [\mathbf{N}_t^e] dV + \int_{\Omega_0^e} k [\mathbf{B}_t^e]^T [\mathbf{B}_t^e] dV \quad (\text{A.8})$$

$$- \int_{\Omega_0^e} [\mathbf{N}_t^e]^T \langle \mathbf{M}_{n+1}^{e,(k)} \rangle^T \langle \dot{\boldsymbol{\epsilon}}_{n+1}^{e,(k)} \rangle [\mathbf{N}_t^e] dV \quad (\text{A.9})$$

$$- \int_{\Omega_0^e} [\mathbf{N}_t^e]^T \theta_{n+1}^{e,(k)} \left\langle \left(\frac{\partial \mathbf{M}}{\partial \theta} \right)_{n+1}^{e,(k)} \right\rangle^T \langle \dot{\boldsymbol{\epsilon}}_{n+1}^{e,(k)} \rangle [\mathbf{N}_t^e] dV \quad (\text{A.10})$$

$$- \int_{\partial \Omega_0^e \cap \Gamma_{N,0}^t} [\mathbf{N}_t^e]^T h [\mathbf{N}_t^e] dA. \quad (\text{A.11})$$

To deduce the detailed forms of sensitivities, \mathbf{r}_n^h is divided into discrete linear momentum and energy balances, denoted separately as $\mathbf{r}_{1,n}^h$ and $\mathbf{r}_{2,n}^h$, corresponding to two equations in (12). Consequently, equation (19) can be equivalently rewritten as

$$\begin{aligned} \mathbf{r}_{1,n}^h \left(\mathbf{u}_n^h, \mathbf{u}_{n-1}^h, \mathbf{v}_{n-1}^h, \boldsymbol{\theta}_n^h, \boldsymbol{\theta}_{n-1}^h, \mathbf{u}_n^{his}, \boldsymbol{\theta}_n^{his}, \mathbf{y}, t_n \right) &= \mathbf{0}, \\ \mathbf{r}_{2,n}^h \left(\mathbf{u}_n^h, \mathbf{u}_{n-1}^h, \mathbf{v}_{n-1}^h, \boldsymbol{\theta}_n^h, \boldsymbol{\theta}_{n-1}^h, \mathbf{u}_n^{his}, \boldsymbol{\theta}_n^{his}, \mathbf{y}, t_n \right) &= \mathbf{0}. \end{aligned} \quad (\text{A.12})$$

The element-level matrix-vector forms of $\mathbf{r}_{1,n}^h$ and $\mathbf{r}_{2,n}^h$ are given in Equations (11) and (A.2). Thus, excluding any interelement contributions, the element-level matrices of $\frac{\partial \mathbf{r}_n^h}{\partial \mathbf{u}_{n-1}^h}$, $\frac{\partial \mathbf{r}_n^h}{\partial \mathbf{v}_{n-1}^h}$, $\frac{\partial \mathbf{r}_n^h}{\partial \boldsymbol{\theta}_{n-1}^h}$ are

$$\begin{aligned} \left[\frac{\partial \mathbf{r}_{1,n}^{e,h}}{\partial \mathbf{u}_{n-1}^h} \right] &= -\frac{4}{\Delta t_n^2} [\mathbf{M}_u^e], & \left[\frac{\partial \mathbf{r}_{2,n}^{e,h}}{\partial \mathbf{u}_{n-1}^h} \right] &= \int_{\Omega_0^e} [\mathbf{N}_t^e]^T [\theta_{n+1}^e] [\mathbf{M}_{n+1}^e] \frac{1}{\Delta t_n} [\mathbf{B}_{u2}^e] dV, \\ \left[\frac{\partial \mathbf{r}_{1,n}^{e,h}}{\partial \mathbf{v}_{n-1}^h} \right] &= -\frac{4}{\Delta t_n} [\mathbf{M}_u^e], & \left[\frac{\partial \mathbf{r}_{2,n}^{e,h}}{\partial \mathbf{v}_{n-1}^h} \right] &= \int_{\Omega_0^e} [\mathbf{N}_t^e]^T \theta_{n+1}^e [\mathbf{M}_{n+1}^e] [\mathbf{B}_{u2}^e] dV, \\ \left[\frac{\partial \mathbf{r}_{1,n}^{e,h}}{\partial \boldsymbol{\theta}_{n-1}^h} \right] &= [\mathbf{0}], & \left[\frac{\partial \mathbf{r}_{2,n}^{e,h}}{\partial \boldsymbol{\theta}_{n-1}^h} \right] &= -\int_{\Omega_0^e} [\mathbf{N}_t^e]^T \frac{c_{n+1}^k}{\Delta t_n} [\mathbf{N}_t^e] dV. \end{aligned} \quad (\text{A.13})$$

Assemble Equations (A.13) over the entire domain. The global matrix forms of the sensitivities terms

$$\left[\frac{\partial \mathbf{r}_{i,n}^h}{\partial \mathbf{u}_{n-1}^h} \right] = \mathbf{A}_e \left[\frac{\partial \mathbf{r}_{i,n}^{e,h}}{\partial \mathbf{u}_{n-1}^h} \right], \quad \left[\frac{\partial \mathbf{r}_{i,n}^h}{\partial \mathbf{v}_{n-1}^h} \right] = \mathbf{A}_e \left[\frac{\partial \mathbf{r}_{i,n}^{e,h}}{\partial \mathbf{v}_{n-1}^h} \right], \quad \left[\frac{\partial \mathbf{r}_n^h}{\partial \boldsymbol{\theta}_{n-1}^h} \right] = \mathbf{A}_e \left[\frac{\partial \mathbf{r}_{2,n}^{e,h}}{\partial \boldsymbol{\theta}_{n-1}^h} \right], \quad (\text{A.14})$$

$i = 1, 2$ are obtained. At the element level,

$$\frac{\partial \mathbf{r}_{i,n}^{e,h}}{\partial \mathbf{u}_n^{his}}, \quad \frac{\partial \mathbf{r}_{i,n}^{e,h}}{\partial \boldsymbol{\theta}_n^{his}}, \quad i = 1, 2, \quad (\text{A.15})$$

can be calculated similarly in matrix form by differentiating the fully discretized form in

Equations (11) and (A.2):

$$\begin{aligned}
 \left[\frac{\partial \mathbf{r}_{1,n}^{e,h}}{\partial \mathbf{u}_n^{his}} \right] &= - \int_{\Omega_0^e} [\mathbf{B}_u^e]^T \left[\left(\frac{\partial \boldsymbol{\sigma}}{\partial \boldsymbol{\epsilon}} \right)_{n+1}^e \right] [\mathbf{B}_{u2}^e] dV , \\
 \left[\frac{\partial \mathbf{r}_{1,n}^{e,h}}{\partial \boldsymbol{\theta}_n^{his}} \right] &= \int_{\Omega_0^e} [\mathbf{B}_u^e]^T \left[\left(\frac{\partial \boldsymbol{\sigma}}{\partial \boldsymbol{\theta}^{his}} \right)_n^e \right] [\mathbf{N}_t^e] dV , \\
 \left[\frac{\partial \mathbf{r}_{2,n}^{e,h}}{\partial \mathbf{u}_n^{his}} \right] &= \int_{\Omega_0^e} [\mathbf{N}_t^e]^T \left[\left(\frac{\partial c}{\partial \mathbf{u}^{his}} \right)_{n+1}^e \right] \dot{\theta}_n^e [\mathbf{B}_{u2}^e] dV - \\
 &\quad \int_{\Omega_0^e} [\mathbf{N}_t^e]^T \theta_n^e \left[\left(\frac{\partial \mathbf{M}}{\partial \boldsymbol{\epsilon}} \right)_n^e \right] [\dot{\boldsymbol{\epsilon}}_n^e] [\mathbf{B}_{u2}^e] dV , \\
 \left[\frac{\partial \mathbf{r}_{2,n}^{e,h}}{\partial \boldsymbol{\theta}_n^{his}} \right] &= \int_{\Omega_0^e} [\mathbf{N}_t^e]^T \left[\left(\frac{\partial c}{\partial \boldsymbol{\theta}^{his}} \right)_n^e \right] \dot{\theta}_n^{e,(k)} [\mathbf{N}_t^e] dV \\
 &\quad - \int_{\Omega_0^e} [\mathbf{N}_t^e]^T \theta_n^e \left\langle \left(\frac{\partial \mathbf{M}}{\partial \boldsymbol{\theta}^{his}} \right)_n^e \right\rangle^T \langle \dot{\boldsymbol{\epsilon}}_n^e \rangle [\mathbf{N}_t^e] dV .
 \end{aligned} \tag{A.16}$$

par This primal sensitivity framework can be applied potentially to any time-step independent and differentiable process parameters. As an example, if the framework is applied to the convection coefficient h , which can be considered a constant, the corresponding element-level sensitivity of (22) is

$$\begin{aligned}
 \left[\frac{\partial \mathbf{r}_{1,n}^{e,h}}{\partial h} \right] &= \mathbf{[0]} , \\
 \left[\frac{\partial \mathbf{r}_{2,n}^{e,h}}{\partial h} \right] &= \int_{\Gamma_{N,0}^t \cap \partial \Omega_0^e} [\mathbf{N}_t^e]^T ([\boldsymbol{\theta}_\infty] - [\boldsymbol{\theta}_n^e]) dA .
 \end{aligned} \tag{A.17}$$

Assembling Equation (A.17) over the entire domain and the matrix form of $\frac{\partial \mathbf{r}_n^h}{\partial \mathbf{y}}$ is obtained.